Enhancing strength and ductility of Al-matrix composite via a dual-heterostructure strategy

Jinfeng Nie [a,1,*], Yuyao Chen [a,1], Lei Song [a], Yong Fan [a], Yang Cao [a,*], Kewei Xie [b], Sida Liu [c], Xiangfa Liu [b], Yonghao Zhao [a,*], Yuntian Zhu [d,*]

[a] *Nano and Heterogeneous Materials Center, School of Materials Science and Engineering, Nanjing University of Science and Technology, Nanjing 210094, China*
[b] *Key Laboratory for Liquid–Solid Structural Evolution and Processing of Materials, Ministry of Education, Shandong University, Jinan 250061, China*
[c] *Laboratory for multiscale mechanics and medical science, SVLAB, School of Aerospace, Xi'an Jiaotong University, Xi'an 710049, China*
[d] *Department of Materials Science and Engineering, City University of Hong Kong, Hong Kong, China*

ARTICLE INFO

ABSTRACT

Aluminum matrix composites (AMCs) often have low ductility, which has been a long-lasting issue in the last few decades. This problem arises largely from the non-deformability of reinforcement particles, which leads to premature failure of the matrix-particle interfaces. Here we propose a new microstructural design strategy for AMCs: distribute the reinforcement particles non-uniformly to form dual-heterostructured AMCs. The zones with high-density particles are recognized as the hard zones, which carry less plastic strain than the particle-free zones to prevent premature interfacial failure. A dual-heterostructured Al-matrix nanocomposite is fabricated, in which AlN nanoparticles are distributed in a dual-level hierarchy: first level heterogeneous nanoparticle distribution and second level heterogeneous zones with different grain sizes. The dual heterostructure produced a unique dual level hetero-deformation induced (HDI) strengthening and hardening to produce high strength and ductility. The dual level HDI strengthening effect has been revealed by the inflection points on the loading-unloading-reloading stress-strain curves. Furthermore, the evolution of local strain fields during the in-situ tensile deformation directly proved the occurrence of strain partitioning, in which the ductile particle free zones have carried a larger strain than the hard particle rich zones. Dispersive shear strain bands are observed for the first time in AMCs. These findings are expected to help design other metal matrix composites with superior mechanical properties.

1. Introduction

Advanced metal matrix composites (MMCs) with high strength, large ductility and good thermal stability, such as particle reinforced Al-matrix composites, are of technological importance for automobile and aerospace industries (Dong et al., 2021; Geng et al., 2023; Ma et al., 2023; Nie et al., 2020; Sun et al., 2022), owing to their light weight and good comprehensive properties (Chen et al.,

---

* Corresponding authors.
  E-mail addresses: niejinfeng@njust.edu.cn (J. Nie), y.cao@njust.edu.cn (Y. Cao), yhzhao@njust.edu.cn (Y. Zhao), yuntizhu@cityu.edu.hk (Y. Zhu).
[1] These two authors contributed equally to this work

2022; Dong et al., 2021; Li et al., 2015a,b; Ma et al., 2023; Yang et al., 2020; Zhang et al., 2022). However, MMCs usually have low ductility which has been a long-lasting issue since the incipient of the MMCs field and has severely limited their applications. The conventional paradigm for designing particle reinforced MMCs is to uniformly distribute the reinforcement particles (Chen et al., 2015; Liu et al., 2018a,b; Najimi and Shahverdi, 2017; Nie et al., 2021; Wang et al., 2023; Zhang et al., 2022). Yield strength is affected by the particle-dislocation interactions, i.e., the Orowan mechanism (Kang and Chan, 2004; Orowan, 1947). For instance, ceramic particles are plastically nondeformable, dislocations thus have to bypass the particles and leave dislocation loops around particles. By decreasing the distance between particles, the overall resistance to dislocation motion is increased, resulting in the strengthening effect (Ma et al., 2014; Aikin, 1991). As the stress concentration builds up at the interfaces between particles and the matrix during the plastic deformation of the matrix, voids can quickly nucleate at interfaces and coalesce into cracks, resulting in premature failure of the bulk MMCs (Jiang et al., 2015). This is why a particle often sits at the bottom of each dimple revealed in the fractography of MMCs (Derrien et al., 1999; Kim, 2006). Apparently, interfacial failure is one of the major limiting factors for the ductility of MMCs. To prevent interfacial failure, it is necessary to limit the plastic strain of the metal matrix, which is paradoxical to the desire for high ductility.

In recent years, heterostructured (HS) materials become an emerging class of materials with superior properties that are unattainable by their conventional homogeneous counterparts (Hasan et al., 2019; Seok et al., 2016; Sitarama Raju et al., 2013; Teng et al., 2023; Wu et al., 2021; Xia et al., 2022; Zhong et al., 2022; Zhu, 2021a; Zhu et al., 2021b). Generally, HS materials consist of ductile zones and hard zones with dramatically different flow stresses. This leads to strain partitioning with the ductile zone carrying a larger fraction of applied strain than the hard zone. A strain gradient will develop near the zone interface to accommodate the strain partitioning, which needs to be accommodated by geometrically necessary dislocations (GNDs) (Gao, 1999), thereby leading to the hetero-deformation induced (HDI) work hardening and HDI stress strengthening (Zhu and Wu, 2019). Many experiments have demonstrated that the yield strength and work hardening capability of metallic materials can both be enhanced by the HDI stress, thereby achieving an extraordinary strength-ductility combination. For example, Wu et al. (2015) have achieved a strength-ductility synergy in a bimodal lamella Ti that exhibits both ultrafine-grained strength and coarse-grained ductility. It is observed that the strain hardening rate in a bimodal lamella Ti is much higher than that of the coarse-grained (CG) sample. The strong strain hardening ability originates from the large HDI stress of up to 600 MPa induced by the heterogeneous lamella structure. Huang et al. (2018) measured the higher HDI stress ranging from 200 MPa to 300 MPa in heterogeneous micrometer-grained Cu/nano-grained bronze laminates. Teng et al. (2023) achieved strength-ductility synergy in graphene nanosheet-reinforced Al-Cu-Mg composites. They claimed that HDI hardening and nano-precipitation strengthening were mainly responsible for the strength-ductility synergy. However, the reinforcement graphene is 2-dimensional inclusion which is different from conventional 3-dimentional nanoparticles.

We hypothesize that this heterogeneous structure strategy can be used to solve the low ductility issue of particle reinforced MMCs. Specifically, contrary to the conventional paradigm, we purposely distribute the ceramic particles heterogeneously, forming hard zones with high-densities of particles and ductile zones without particles. We envision that due to the strain partitioning the hard zones will carry lower plastic strain to prevent particle-matrix interfacial failure, while the ductile zones will sustain higher plastic strain to produce high ductility. The HDI stress strengthening will act to maintain a high yield strength while the HDI work hardening will help to improve ductility.

Massive dislocation emission at a crack tip due to local stress concentration can inhibit crack propagation, resulting in the effect of crack blunting (Horton, 1982; Rice and Thomson, 2006). Ovid'ko and Sheinerman (2009; 2010) reported that the effectiveness of cracks blunting at room temperature is very sensitive to the grain size. This is because grain boundaries will inhibit dislocation emission by exerting back-stress to shut down the dislocation source and thus to lessen crack blunting. Moreover, cracks tend to propagate along grain boundaries, causing deflection of cracks. Actually, some tentative studies were reported in the past few years and found that MMCs with an inhomogeneous discrete distribution of reinforcement tend to exhibit a higher damage tolerance (energy absorption capability), which was only understood in view of the plastic regions blunting or deflecting cracks after necking. For example, Huang et al. (2015) designed and fabricated a network-distributed TiB whiskers reinforced titanium matrix composite, and this tailored three-dimensional quasi-continuous network microstructure significantly improved the mechanical properties of the composite. The large reinforcement-lean regions can bear the strain, blunt cracks and prevent crack extension, thus remarkably improving the ductility of the composite. Luo et al. (2022) proposed an inverse nacre structure for magnesium matrix nanocomposite, where elongated and curled soft constituents (Mg) are embedded in hard constituents (SiC nanoparticle reinforced Mg matrix); It enables microcrack-multiplication process to help sustain a high ultimate tensile strength. Despite the abovementioned advances, most aluminum matrix composites (AMCs) with inhomogeneous particle distributions exhibit elongations of only ~2 % (Jiang et al., 2016), which are still far below the desired requirement of elongation (>5 %) for engineering applications. In fact, the crucial design principle, intrinsic strengthening and toughening mechanisms in MMCs have not been revealed thoroughly in terms of the physical origin of GNDs at the zone interfaces and its effects on the strain evolution and mechanical behavior. Some current studies have only revealed the deformation mechanisms of AMCs with homogeneous particle distributions or heterogeneous multi-layered (or two-phase) composites (Li et al., 2020a,b; Li et al., 2022; Liu et al., 2022). For example, Rong et al. (2023) investigated the work hardening and strain delocalization in in-situ dense intragranular nanoscale Al_2O_3 reinforced Al-5CuO composites. Results reveal that the intragranular Al_2O_3 can improve the strain partitioning and the strain/stress transfer, which significantly contributes to strain delocalization and hence strength-ductility synergy. When the Al layer thickness was nearly twice that of the interfacial stress-affected zone, Ti/Al layered composites exhibited the highest work hardening rate, the greatest uniform flow capacity, and the most dispersed crack distribution, which synergistically contributed to the excellent comprehensive mechanical properties (Wu et al., 2023) While there is still a lack of systematic research on the deformation mechanism of heterostructured aluminum matrix composites.

To prove the above strategy and reveal the strengthening and toughening mechanism in-depth, we designed a dual-heterostructured Al-matrix nanocomposite characterized by ductile micro-grained Al fibrous zones embedded in ultrafine-grained

(UFG) composite matrix containing high-densities of AlN nanoparticles. We name this a dual-heterostructured composite because it consists of two levels of heterostructures: first level heterogeneous nanoparticle distribution and second level heterogeneous zones with different grain sizes. The dual heterostructure strategy utilized in the current work opens a new route for the development of promising lightweight MMCs.

2. Experimental details

2.1. Sample preparation

AlN$_p$/Al nanocomposites with the same compositions and different microstructures have been prepared by utilizing the in-situ melt reaction method and subsequent thermal-mechanical treatment as schematically illustrated in Figs. 1 and 2. Commercial purity Al powders (99.7 %, all compositions quoted in this work are nominal values in mass fractions unless otherwise stated) with an average particle size of ~20 μm and Boron Nitride powders (99 %) with an average particle size of ~2 μm were used as raw materials to prepare a bulk Al nanocomposite reinforced by 12 % AlN nanoparticles (Fig. 1a). As illustrated in Fig. 1b, the raw powders were mixed and ball milled for 2 h under argon atmosphere. Then the powder mixtures were compressed via cold isostatic pressing at a pressure of 150 MPa. The compact sample was sintered at 700 °C in a vacuum to promote the liquid-solid reaction for the situ formation of AlN nanoparticles (Fig. 1c). The in-situ reaction that occurred in the present experiment has been given in the supplementary materials. The AlN$_p$/Al nanocomposite precursor with a heterogeneous distribution of AlN nanoparticles was obtained after sintering. The precursor sample consists of net-like particle rich zones (PRZs) and irregular particle free zones (PFZs), as illustrated in Fig. 1d. Then the sintered precursor sample was hot extruded at 350 °C to obtain fibrous PFZs (Fig. 1e). Fig. 2 shows the processing route for the bulk nanocomposite and the corresponding microstructural evolution. Fig. 2a is an SEM image showing the typical microstructure of the sintered AlN$_p$/Al nanocomposite precursor. Subsequent hot extrusion stretched the PFZs into fibrous shapes and reshaped PRZs into thick bands, as shown in Fig. 2b. The hot extruded nanocomposite is referred to as the HS1 sample hereafter. The HS1 sample was further subjected to rotary swaging (RS) treatment at room temperature to an equivalent strain of ~0.25 and a subsequent low temperature annealing treatment at 200 °C for 10 min. As a result, a homogenous distribution of AlN nanoparticles in the metal matrix has been obtained as shown in Fig. 2c. Most of the AlN particles are distributed along the a-Al grain boundaries and some particles are also seen at grain interiors. The swaged and annealed sample is referred to as the HS2 sample hereafter.

2.2. Microstructural characterization and tensile properties evaluation

Microstructures of the nanocomposites were characterized by a Quanta 250F scanning electron microscope (SEM), Zeiss Auriga
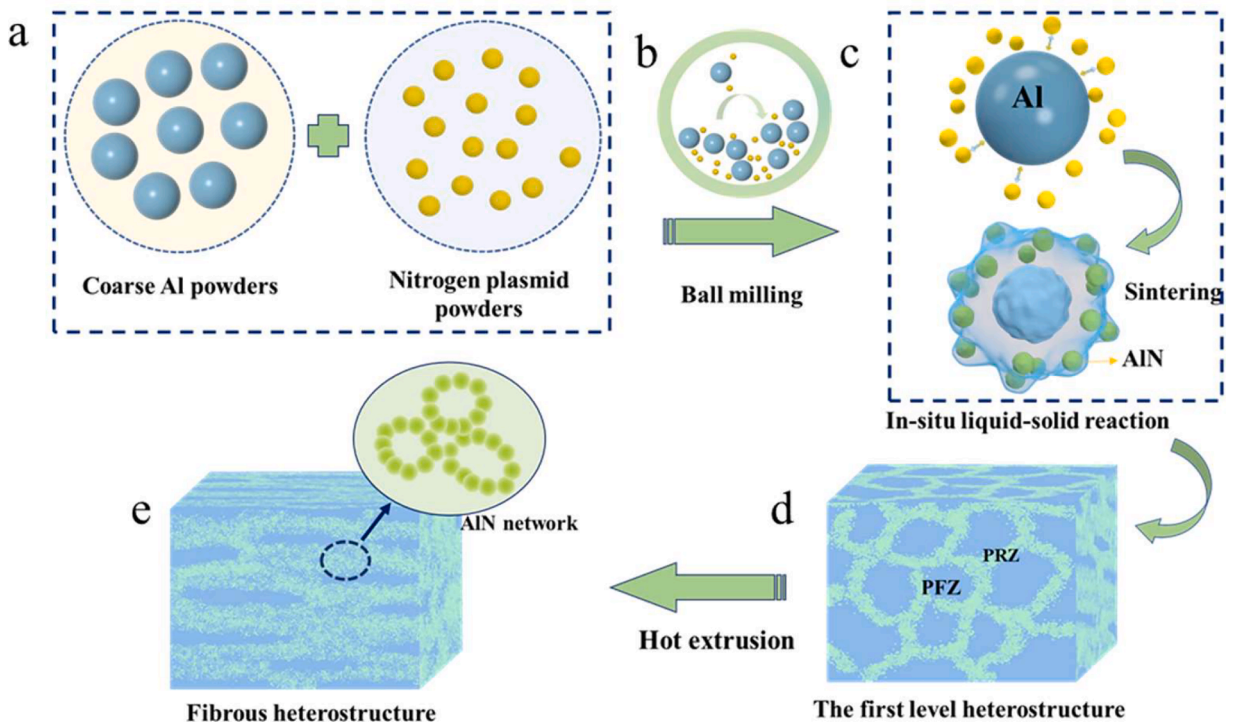
Fig. 1. Schematic illustration of the production process for the heterostructured AlN$_p$/Al nanocomposite.
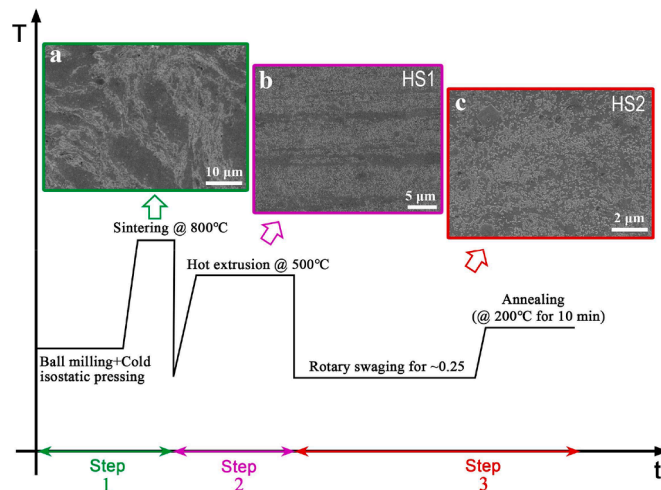
Fig. 2. Microstructural evolution of the AlN$_p$/Al nanocomposite along the processing route.

SEM equipped with the electron backscattered diffraction detector, Tecnai-20 transmission electron microscope and TECNAI-G2-200 aberration-corrected TEM. SEM samples were prepared by mechanical polishing with sand papers, and fine polishing with Struers OP-S colloidal silica suspension. EBSD samples were firstly mechanically polished, and then electro-chemically polished in a solution consisting of 10 % perchloric acid and 90 % ethanol under 20 V applied voltage for 15 s at −20 °C. TEM samples were prepared by the ion beam thinning method: 5 keV acceleration voltage and the beam angle of ∼7° were used for perforation; 3 keV acceleration voltage and the beam angle of ∼4° were used for final trimming. Dog-bone shaped specimens with a gauge length of 10 mm, width of 2.5 mm, and thickness of 1.5 mm, were used for tensile tests. In this work, all tensile tests were performed along the extrusion and rotary swaging directions of the composites. The uniaxial tensile tests were carried out on a Walter-bai-LFM-20 kN universal test machine with a strain rate of $1 \times 10^{-3}\,\mathrm{s}^{-1}$ at ambient temperature. The loading-unloading-reloading (LUR) tensile tests were conducted at the tensile strain rate of $1 \times 10^{-3}\,\mathrm{s}^{-1}$, and a load-controlled unloading rate of 20 N/s to a minimum load of 50 N. A mechanical extensometer was used in all tensile tests.

2.3. DIC characterization

Dog-bone-shaped specimens with a gauge size of $15 \times 2.5 \times 2\ \mathrm{mm}^3$ were prepared for Nakazima tests, namely the strain measurement by digital image correlation (DIC). The sample surface was firstly polished to mirror finish; Then an adhesive and flexible white matte paint was sprayed on the surface; Finally, a high-contrast stochastic pattern of black spots was painted on the specimen for DIC analysis. The displacements of the black spots during the tensile test were recorded by two non-symmetrically positioned CCD cameras, e.g., one camera was located directly in front of the specimen and another camera was positioned approximately 32° to the normal direction of the specimen. Each CCD camera recorded 2 images per second during the tension test. The image set was later analyzed by using the ARAMIS software to deduce the evolution of strain fields.

Furthermore, a MINI-MTS2000 in-situ tensile system was used in conjunction with an SEM-DIC strain measurement system to capture the evolutions of microstructures and the local strains of the bulk nanocomposites under tensile deformation. Nanocomposite samples were etched by 0.5 % HF to reveal high contrast speckle patterns for high quality SEM-DIC analysis. Refined speckle patterns were captured by the secondary electron detector to produce the digital SEM images which were taken after each strain increment. The ARAMIS software was used to analyze the strain field based on the serial SEM images.

3. Results and discussion

3.1. Microstructures of the dual-heterostructured AlN$_p$/Al nanocomposites

Representative microstructures of the HS1 and HS2 samples are presented in Fig. 3. The HS1 nanocomposite exhibits the dual heterostructure consisting of particle rich zones (PRZs) and particle free zones (PFZs) as shown in Fig. 3a1 and a2, which is inherited from the as-sintered composite sample. The interfaces separating the PRZs and PFZs are clean and well bonded. The PFZs are composed of coarse Al grains (3–10 μm), and are elongated along the extrusion direction (ED), as shown in Fig. 3a2. The widths of the elongated PFZs are in the range of 3–13 μm, and the PFZs are spaced apart for 10–30 μm, as shown in Fig. S2 in the supplementary materials. In contrast, there are high densities of nanoparticles in the PRZs and the ultrafine Al grains with grain sizes of 0.5–1.5 μm are seen in the PRZs. The grain size distributions of α-Al grains in the PRZs and PFZs are shown in Fig. 3c1 and c2. The volume fractions of the ductile PFZs and hard PRZs are calculated to be ∼19.3 % and ∼80.7 %, respectively. At a lower magnification, Fig. S2a shows the dual heterostructure of the AlN/Al nanocomposite (HS1 sample) in three dimensions, which clearly illustrates the heterogeneous
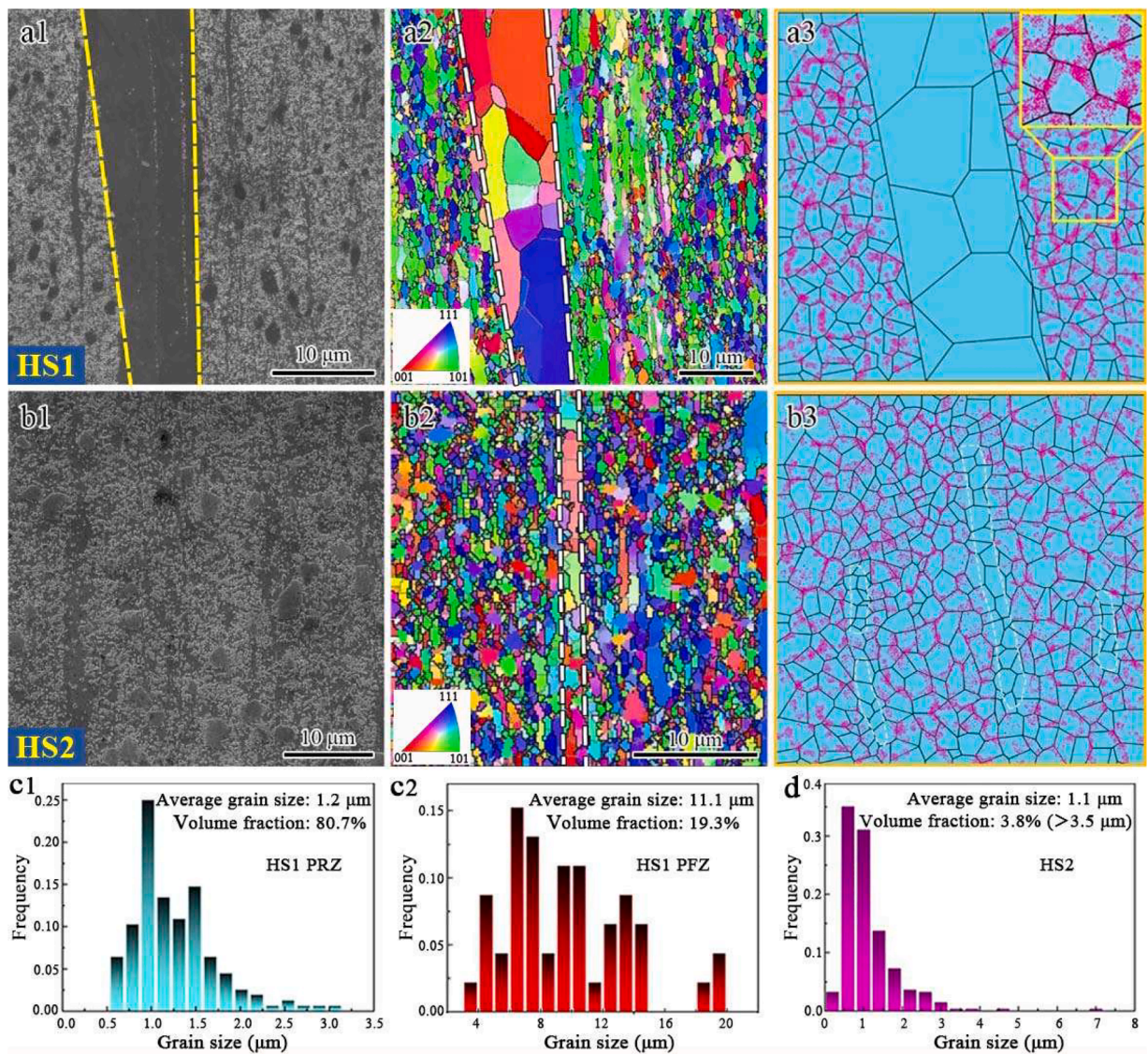
Fig. 3. The microstructures of the two AlN$_p$/Al nanocomposites: (a1, b1) SEM images showing the diverse particle distributions in HS1 and HS2 samples, (a2, b2) Inverse pole figure EBSD maps revealing the matrix grain structure of HS1 and HS2 samples, (a3, b3) schematic diagrams illustrating dual heterostructure and normal heterostructure, (c1, c2) statistics of the grain size distributions in the PRZs and PFZs of HS1 samples, (d) grain size distributions in HS2 samples.

distribution of AlN nanoparticles in the matrix. At higher magnification (Fig. S2b), the particles with an average particle size of ~95.3 nm in the PRZ zones distributed more homogenously in the HS1 nanocomposite than the as-sintered one. As shown in the schematic diagram in Fig. 3a3, black lines represent grain boundaries and pink dots represent AlN particles. The dual heterostructure of the HS1 sample consists of PRZs and PFZs. AlN particles agglomerate to form networks in the PRZs. The Al grains in the PRZs are significantly smaller than those in the PFZs. In the HS1 sample, both AlB$_2$ particles and AlN nanoparticles formed during the sintering process are found by SEM-EDS mapping as shown in Fig. S1 in the supplementary material. The sizes of AlB$_2$ particles are ~0.8–2.5 μm, and the density of AlB$_2$ particles is much smaller than that of AlN nanoparticles.

The extruded HS1 samples were further subjected to rotary swaging (RS) and low-temperature annealing treatment to obtain the HS2 samples. RS is a high-speed and high-pressure process. During the RS process, the composite sample is exposed to complex deformation modes with cyclic compressive shear stresses in both axial and radial directions. High strain rates and multiaxial stress state may cause dynamic recrystallization, which in the current case may help with making recrystallized fine grains in the particle free zones (PFZs) in the HS2 sample. On the other hand, the second phase particles are nondeformable but may flow with the matrix material during the RS process, resulting in a dispersion of the second phase particles (Chen et al., 2023). It is well known that second phase particles increase the shear strain in nearby regions, inducing the formation of deformation zones around the particles, or even promoting dynamic recrystallization during plastic deformation. Therefore, dispersed particles in the aluminum matrix also contribute

to the refinement of the grain structure of matrix. As the AlN particles are mechanically dispersed, they move into the original PFZs and thus to help refine the Al grains in the PFZs, as shown in Fig. 3b1 and b2. Consequently, the volume fraction of PFZs was decreased. The Al grain structures are homogeneous, although there are still the same randomly distributed thin ribbons (one is traced by dashed lines in Fig. 3b2) of coarse grains which are inherited from the PFZs in the HS1 sample. The overall microstructure of the HS2 sample is illustrated in Fig. 3b3. The Al grain size distribution for the HS2 sample is given in Fig. 3d. The volume fraction of the ductile PFZs was reduced significantly from ~19.3 % to 3.8 % for the HS2 nanocomposite. Both the HS1 and HS2 samples exhibit $\{111\}_{Al}$ fiber texture, i.e., $\langle 111 \rangle_{Al}//ED$ (Fig. S3).

Fig. 4 shows the TEM images of the dual-heterostructured AlN_p/Al nanocomposite (HS1). As shown in Fig. 4a and b, the coarse and elongated Al grains are sandwiched between UFG PRZs. Fig. 4c is a TEM image showing AlN nanoparticles with sizes of approximately 30–90 nm. The nanoparticles formed continuous and semi-continuous networks in the UFG Al matrix. Fig. 4d is a high resolution TEM image showing lattice fringes for an AlN particle submerged in an Al grain; The clean and well-bonded AlN_p/Al interface can be observed. The areas enclosed by the yellow and red dotted squares in Fig. 4d are enlarged and shown in Fig. 4d1 and d2, respectively. As shown in Fig. 4d, AlN_p and Al have an orientation relationship of $(10\bar{1}1)_{AlN}//(111)_{Al}$, suggesting that a coherent interface is formed between them.

The microstructure of the HS2 sample is analyzed for details by SEM and TEM. Fig. 5a is a high resolution SEM image showing AlN nanoparticles with an average particle size of ~86.2 nm submerged in the Al matrix in the HS2 sample. Fig. 5b and c are TEM images also showing AlN nanoparticles with sizes less than ~100 nm (indicated by the yellow arrows in Fig. 5c). Fig. 5d is a high resolution TEM image showing lattice fringes of AlN nanoparticles and the Al matrix. The AlN_p/Al interfaces are still intact, suggesting that RS treatment did not induce any cracks along the AlN_p/Al interfaces. In addition, the dislocation densities in the HS1 and HS2 nanocomposites are calculated based on the EBSD and XRD data and are provided in Table 1. According to literature (Wauthier-Monnin et al., 2015; Gallet et al., 2023), EBSD and XRD detect GNDs and statistically stored dislocations (SSDs), respectively. Knowing that the accuracies of dislocation densities measurement by EBSD and XRD are affected by many factors and parameters (Wauthier-Monnin et al., 2015; Gallet et al., 2023; Calcagnotto et al., 2010; Bate et al., 2005), the dislocation density data is considered indicative rather than determinative. The dislocation density (both XRD and EBSD measurements) of the HS1 sample is slightly lower than that of the HS2 sample. Apparently, in addition to the slightly increased dislocation density, the major work done by RS treatment plus
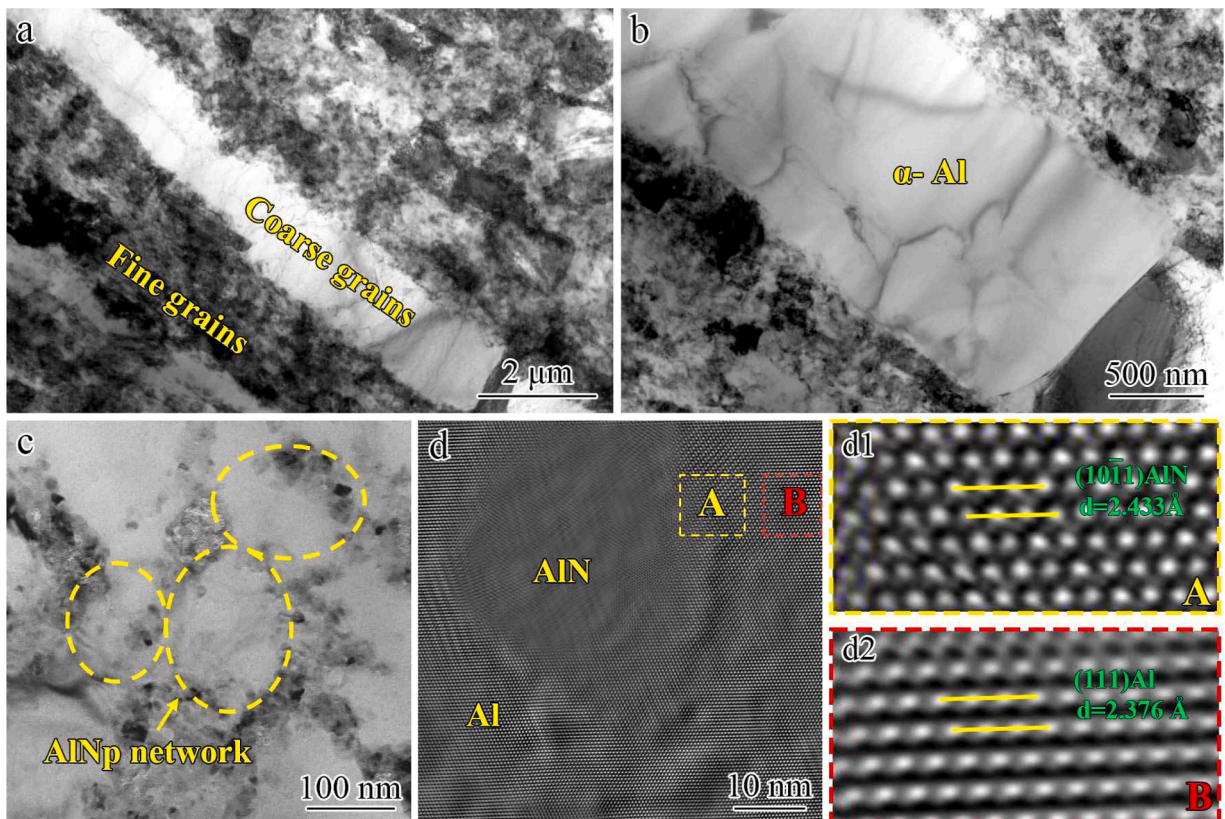
Fig. 4. TEM characterization of the dual-heterostructured AlN_p/Al nanocomposite (HS1): (a, b) a bright-field image showing the coarse-grained (CG) PFZ sandwiched between UFG PRZs, (c) networks formed by nanoparticles traced by the yellow dotted circles, (d) a high resolution TEM image showing an AlN particle in the Al matrix, (d1, d2) the enlarged high resolution TEM images of the two regions enclosed by the yellow and red dotted squares in (d). (For interpretation of the references to colour in this figure legend, the reader is referred to the web version of this article.)
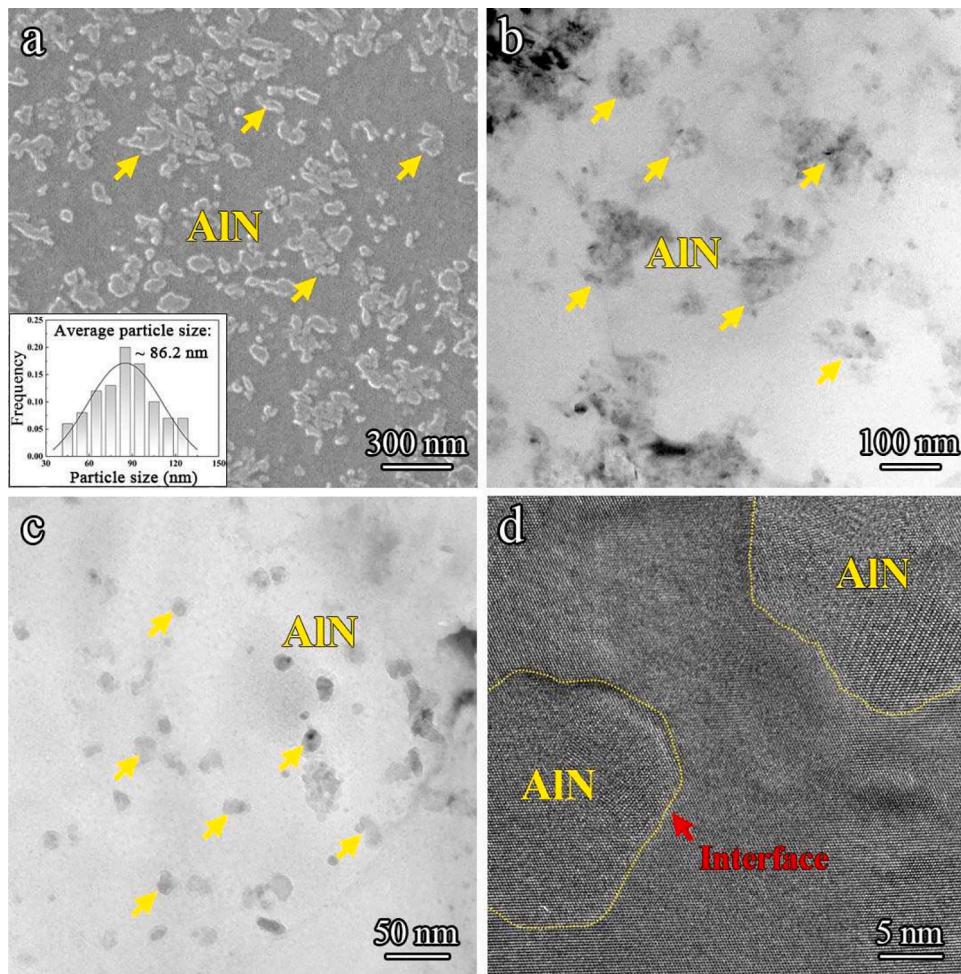
Fig. 5. Microstructures in the HS2 AlN$_p$/Al nanocomposite: (a) SEM image showing AlN nanoparticles in the Al matrix, (b, c) TEM images showing the dispersion of AlN nanoparticles, (d) High resolution TEM image showing lattice fringes of AlN particles and the Al matrix. Inset in (a) shows the particle size distribution.

Table 1
Dislocation densities of two AlN$_p$/Al nanocomposites calculated by XRD and EBSD data.

Samples	ρ (m^{-2}) XRD	ρ_{GND} (m^{-2}) EBSD
HS1	$(2.64 \pm 0.82) \times 10^{14}$	$(2.10 \pm 0.43) \times 10^{14}$
HS2	$(4.90 \pm 0.53) \times 10^{14}$	$(2.86 \pm 0.71) \times 10^{14}$

low-temperature annealing was to refine the Al grains and homogeneously distribute the AlN nanoparticles.

3.2. Tensile properties of ALN$_p$/Al nanocomposites

Fig. 6a shows the tensile engineering stress-strain curves for the HS1 and HS2 nanocomposites along the ED. The HS2 nanocomposite reinforced by homogeneously dispersed nanoparticles, shows a high yield strength (YS) of ~338 MPa, an ultimate tensile strength (UTS) of ~374 MPa, a very low uniform elongation (ε_u) of ~0.9 % and an elongation to failure (ε_f) of only ~1.7 %. Although the YS of HS2 is nearly three times higher than that of the CG pure Al, it comes with a dramatic loss of ductility. In contrast, the HS1 nanocomposite with the dual heterostructure demonstrates the mechanical properties: YS = ~346 MPa, UTS = ~419 MPa, ε_u = ~4.4 % and ε_f = ~9.2 %. This result is remarkable, as the ε_u of the HS1 sample is improved by nearly five times to the HS2 sample, while both YS and UTS are also improved. Apparently, HS1 nanocomposite with the dual heterostructure achieves an outstanding strength-ductility combination. The mechanical properties of HS1, HS2 and CG Al samples are listed in Table 2 for the reader's convenience. In addition, the tests on mechanical properties of HS1 and HS2 nanocomposites perpendicular to the extrusion/rotary swaging
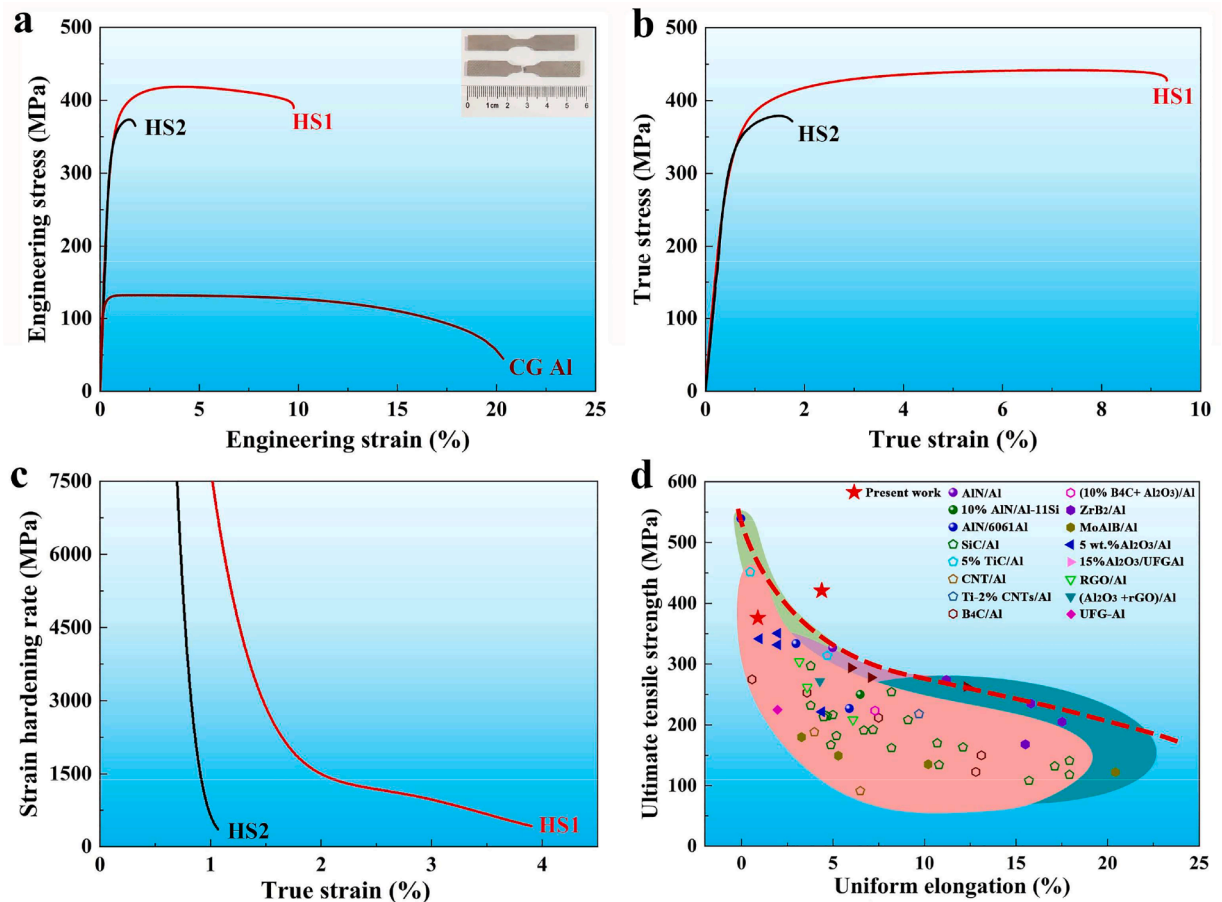
Fig. 6. (a) Engineering stress-strain curves for HS1, HS2 and CG Al samples along the ED. (b) True stress-strain curves for the HS1 and HS2 nanocomposites. (c) Plots of strain hardening rates for the HS1 and HS2 nanocomposites. (d) Comparison of heterostructured AlN$_p$/Al nanocomposites with other aluminum matrix composites (AMCs) for strength versus uniform elongation (Ashok Kumar and Murugan, 2012; Ding et al., 2022; Fattahi et al., 2015; Guo et al., 2020; Hu et al., 2008; Kai et al., 2019; Li et al., 2020a,b; Li et al., 2015a,b; Liu et al., 2020a,b; Mavlyutov et al., 2017; Ren et al., 2022; Shen et al., 2020; Wahab et al., 2011; Xing et al., 2022; Yu et al., 2011; Zan et al., 2019, 2020; Zhang et al., 2021). The reader is referred to Table S1 in the supplementary material for the mechanical properties of AMCs.

direction (i.e., transverse direction, TD) were also carried out. The tensile engineering stress-strain curves along the ED and TD directions are compared in Fig. S4 in the supplementary materials. Apparently, the strength and ductility along the ED are significantly better than those along TD, indicating that the particular types of heterostructures only provide superior tensile properties along the ED.

Comparing the mechanical properties, microstructures and defect densities of the HS1 and HS2 samples reveals several unique findings that cannot be directly explained by the conventional materials science in the textbooks: First, as shown in Fig. 3c1 and c2, the HS1 sample has a larger volume fraction of ductile PFZs, and larger grains in the matrix than the HS2 sample; However, the HS1 sample has a higher YS than the HS2 sample, that seems to violate the Hall-Petch relationship and the rule of mixtures. Second, according to Table 1, the measured dislocation densities in the HS1 and HS2 samples reveal $\rho_{HS2} > \rho_{HS1}$; However, the HS1 sample has higher YS than the HS2, which seems to violate the Taylor equation (Gao, 1999; Zhu, 2021a): $\sigma_{0.2} = \alpha Gb\sqrt{\rho}$, where α is a constant, G is the shear modulus, and b is the Burgers vector. Third, the HS1 sample has both higher strength and higher ductility than the HS2 sample, avoiding the strength-ductility trade-off. Provided that the classic equations mentioned above have long been proven correct, there must be reasonable explanations for the apparent violations which will be discussed later.

Table 2
The tensile properties of the AlN$_p$/Al nanocomposites and CG Al.

Materials	Yield strength (YS/MPa)	Ultimate tensile strength (UTS/MPa)	Elongation to failure (ε_f/%)	Uniform elongation (ε_u/%)
HS1	346 ± 5	419 ± 3	9.2 ± 0.6	4.4 ± 0.3
HS2	338 ± 3	374 ± 3	1.7 ± 0.2	0.9 ± 0.1
CG Al	121 ± 4	132 ± 6	20.3 ± 1.5	4.1 ± 0.8

These observations indicate a strong heterostructure effect in the HS1 sample (Wu et al., 2015; Zhu et al., 2021b; Zhu and Wu, 2019), which is further demonstrated by the improved strain hardening behavior. Fig. 6c shows the strain-hardening rate ($\Theta = d\sigma/d\varepsilon$) versus true strain curves for the HS1 and HS2 nanocomposites. Θ drops quickly for the HS2 nanocomposite, leading to low ductility. The HS1 nanocomposite has much higher strain hardening rates than the HS2 nanocomposite for the entire plastic deformation, which can contribute to the higher ductility. The observed high strain hardening rates in the HS1 nanocomposites are undoubtedly derived from the unique dual heterostructure. Fig. 6d shows a comparison of tensile properties of the dual-heterostructured AlN_p/Al nano-composite with those of reported aluminum matrix composites (AMCs) (Ashok Kumar and Murugan, 2012; Ding et al., 2022; Fattahi et al., 2015; Guo et al., 2020; Hu et al., 2008; Kai et al., 2019; Li et al., 2020a,b; Li et al., 2015a,b; Liu et al., 2020a,b; Mavlyutov et al., 2017; Ren et al., 2022; Shen et al., 2020; Wahab et al., 2011; Xing et al., 2022; Yu et al., 2011; Zan et al., 2019, 2020; Zhang et al., 2021). Most of the AMCs are in the dilemma of the strength-ductility trade-off. In contrast, the dual-heterostructured AlN_p/Al nanocomposite (HS1) stands out from the trend, suggesting a superior strength-ductility combination.

3.3. Discussion

3.3.1. Evolution of the dual heterostructure

The heterogeneous particle distribution and the resultant PRZs and PFZs formed under the preliminary sintering process, as shown in Fig. 7. The ductile PFZs are surrounded by the hard PRZs as shown in Fig. 7a. This microstructure is akin to the core-shell structure, and is a crucial feature to guarantee the strong heterostructure effect (Chen et al., 2015; Ma et al., 2023; Sun et al., 2022). The heterogeneous particle distribution is formed due to the in-situ liquid-solid reaction of coarse Al particles (~20 μm) with nitrogen boron particles (~2 μm). It is noted that the sintering process took place at 700 °C (above the melting temperature 660 °C of Al) to activate the in-situ liquid-solid reaction, during which the majority of the Al particles with an average size of ~20 μm melted and recrystallized into Al grains of millimeter size. Fig. 1 schematically shows that most nitrogen boron particles are attached to the surface of Al particles during the ball-milling process and reacted with the Al powders at the surfaces during sintering, to form a transition shell surrounding the large aluminum particles. Due to the low mobility of the in-situ-formed AlN nanoparticles in the Al melt, it is hard for these nanoparticles to disperse uniformly in the melt. As shown in Fig. 7e and f, most AlN nanoparticles are in touch with one another to form continuous and semi-continuous networks. It is considered that the continuous particle network can produce better strengthening than uniformly dispersed particles (Shao et al., 2019; Wang et al., 2022). Consequently, the PFZs and PRZs formed after solidification as shown in Fig. 7a and d.

Although the PFZs and PRZs have formed in the sintered sample, the Al grain sizes in the millimeter range are very large. The subsequent hot extrusion process effectively made particle redistribution and grain refinement to make the bulk sample HS1. During the hot extrusion process, the PFZs were stretched along the ED. The widths of PFZs were narrowed to 3–13 μm and the inter-PFZs
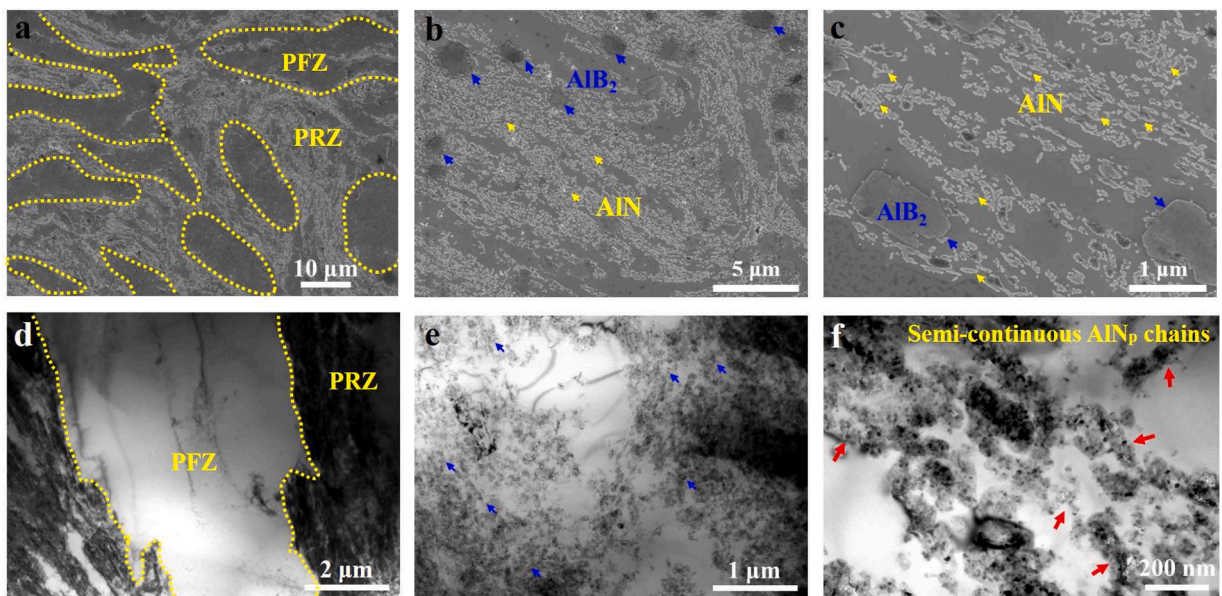
Fig. 7. Microstructures of as-sintered AlN_p/Al nanocomposites: (a) heterogeneous distribution of AlN nanoparticles and the particle free zones (PFZs)/particle rich zones (PRZs) interfaces indicated by the yellow dash lines, (b, c) SEM image showing the morphology and distribution of AlN nanoparticles of AlN_p/Al nanocomposite at higher magnification as well as a small amount of AlB_2 particles with 1–2.5 μm formed in the matrix, (d) TEM image showing the heterostructure of the composites, (e) TEM image of the particle distribution in the PRZs, (f) a magnified TEM image showing the semi-continuous nanoparticles chains and networks in the matrix. The PFZs evolved into the elongated coarse grains after hot extrusion, and then the PRZs evolved into the ultrafine-grained structure. (For interpretation of the references to colour in this figure legend, the reader is referred to the web version of this article.)

spacing is about 10–30 μm as shown in Figs. 3a1 and S2a in the supplementary material. As shown in the high magnification SEM image of Fig. S2b, the particles in the PRZs distributed more homogenously in the HS1 sample than the as-sintered one (Fig. 7b, c). On the other hand, the dispersion of nanoparticles also helps form the heterogenous Al grain structure, by exerting the pinning effects on dislocations and boundaries (Nie et al., 2021). Thus, by conducting hot extrusion the Al grains in the PFZs and PRZs have been significantly refined to sizes of 3–10 μm and 0.5–1.5 μm, respectively. The hot extruded HS1 sample thus possesses the desired dual heterostructure consisting of heterogeneous nanoparticle distribution and heterogeneous zones with different grain sizes. Because the HS1 sample demonstrated the best strength-ductility combination among all the samples of study, as shown in Fig. 6; It is anticipated that the unique dual heterostructure configuration can produce effective hetero-deformation induced (HDI) strengthening and hardening for the superior combination of mechanical properties (Wu et al., 2015; Zhu et al., 2021b).

3.3.2. HDI hardening effect in dual heterostructure

Loading-unloading-reloading (LUR) tests along the ED were conducted to evaluate the stress state in the dual heterostructure. As shown in Fig. 8a and b, both LUR curves for HS1 and HS2 samples exhibit hysteresis loops attributed to the Bauschinger effect (Liu et al., 2018a,b; Xiang and Vlassak, 2005). In contrast, the CG Al shows negligible stress-strain hysteresis as shown in Fig. 8a. As reported in the literature (Wu et al., 2015; Zhu and Wu, 2019), the flow stress can be divided into HDI stress (σ_{HDI}) associated with the geometrically necessary dislocations (GNDs) and the effective stress (σ_{eff}) for dislocation slip. Plastic deformation in the heterostructure is heterogeneous but continuous, producing strain gradients near the zone boundaries, which need to be accommodated by GNDs. The accumulations of GNDs lead to strong back stresses in the ductile zones, which could offset the applied stress, making the ductile zone appear stronger. The back stress in the ductile zone in turn induces forward stress in the hard zone. The back stress and forward stress collectively produce the HDI strengthening and hardening (Zhu and Wu, 2019). The HDI hardening on top of other known hardening effects is crucial to achieve an excellent strength-ductility combination.

As shown in Fig. 8b, the HDI stress can be calculated as (Yang et al., 2016; Zhu and Wu, 2019):
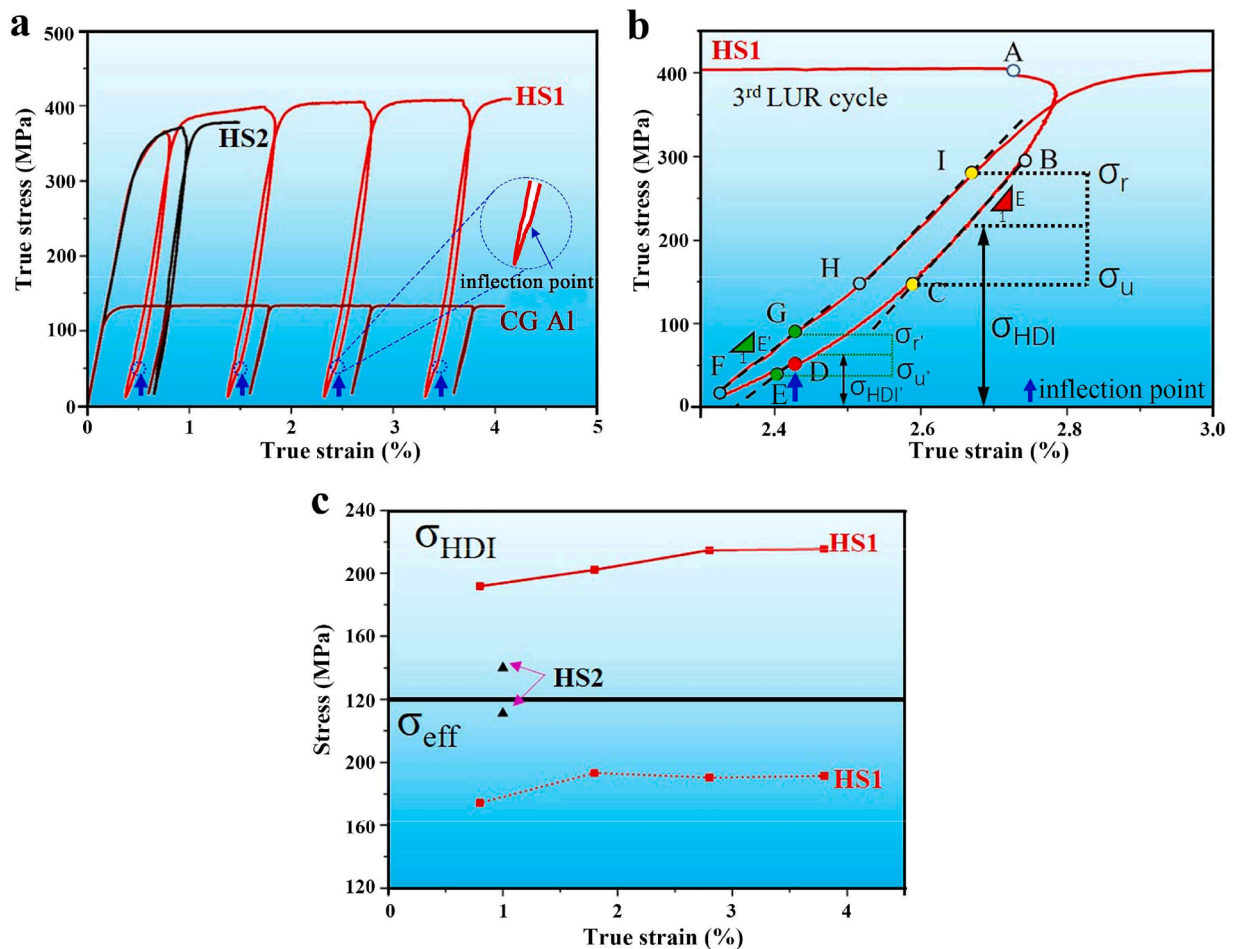
Fig. 8. Determination of HDI stress in heterostructured nanocomposites: (a) LUR stress-strain curves for HS1, HS2, and CG Al, (b) enlarged view of a hysteresis loop of HS1 for determining the HDI stress, (c) σ_{HDI} and σ_{eff} versus true strain.

$$\sigma_{HDI} = (\sigma_u + \sigma_r)/2 \tag{1}$$

where σ_u and σ_r are the unloading yield point and reloading yield point, respectively. Then, the σ_{eff} can be calculated as:

$$\sigma_{eff} = \sigma_{flow} - \sigma_{HDI} \tag{2}$$

σ_{HDI} and σ_{eff} for the samples are calculated at different true strains and plotted in Fig. 8c. Fig. 8c shows that the HDI stress increases with increasing strain for HS1 and is much higher than those of HS2. Therefore, the heterostructure of the HS1 sample is more effective in producing HDI strengthening than that of the HS2 sample. The HDI stress is about 200 MPa near the yield point for the HS1 sample. Fig. 8c shows that $\sigma_{HDI} > \sigma_{eff}$ for the HS1 sample, but $\sigma_{HDI} < \sigma_{eff}$ for the HS2 sample. Hence, HDI strengthening is very strong in the HS1 sample, but comparatively weak in the HS2 sample. These observations clearly demonstrate that the unique dual heterostructure configuration in HS1 is far more effective in generating HDI strengthening than the uniform dispersion of nanoparticles in the metal matrix.

As indicated by the blue arrows in Fig. 8a, there is an inflection point at which a sudden change of the slope occurs for each hysteresis loop. To our knowledge, inflection points on hysteresis loops have never been reported for heterostructured materials, and can only be explained by the dual heterostructure configuration in HS1. Firstly, the unloading starts at point A in Fig. 8b. The segment AB on the unloading curve is quasi-elastic and is caused by stress relaxation (Dickson et al., 1984) or viscous flow of the materials (Fournier et al., 2006a, 2006b). The segment BC is the linear (elastic) part of the unloading stress-strain curve with a slope of E. The point of C corresponds to the unloading yield point (σ_u), and the HDI stress starts to overcome the applied stress and the frictional stress (σ_f) to make GNDs glide backward, i.e. (Yang et al., 2016):

$$\sigma_{HDI} = \sigma_u + \sigma_f \tag{3}$$

It is noteworthy that the frictional stress (σ_f) is always in the direction that opposes the motion of dislocations. The frictional stress can be regarded as the isotropic strengthening resistance, which consists of the Peierls stress as well as other stresses that are needed to overcome the dynamic pinning of dislocations such as solute atoms, second phase, forest dislocations, dislocation debris, dislocation jogs, etc. (Yang et al., 2016).

During the deformation in the segment BD, excessive GNDs are produced at the zone interfaces of UFG PRZs and CG PFZs. Additionally, due to the hard AlN nanoparticles in the UFG matrix, GNDs will also be produced in the UFG matrix to have a compatible deformation (Yang et al., 2018). Thus, the two levels of the dual heterostructure contributed simultaneously to the overall HDI stress. However, with further unloading after the inflection point D, the slope in the segment DE is reduced significantly. It is reasonable to assume that the contribution of GNDs produced in the UFG matrix decreased to near zero due to the very limited space for dislocation slip in the ultrafine grains. In other words, in the lower segment of the unloading curve, the HDI stress originates largely from the second level heterostructure and is generated near the interfaces between ductile CG PFZs and hard UFG PRZs. Point E is the unique secondary unloading yield point ($\sigma_{u'}$) in the lower segment. At the secondary unloading yield point E, the applied stress is very low, and the HDI stress originating from the second level heterostructure starts to overcome the applied stress and the frictional stress (σ_f) to make dislocation glide backward even further, i.e. (Yang et al., 2016):

$$\sigma_{HDI'} = \sigma_{u'} + \sigma_{f} \tag{4}$$

During the reloading process, the applied stress firstly needs to overcome the frictional stress and the HDI stress (originated from the second level heterostructure), in order to drive dislocations forward again at the reloading yield point G ($\sigma_{r'}$). As the applied stress increases, the slope of the segment HI becomes larger after the point H. The slopes of the segments FG and HI represent the effective reloading Young's modulus resulting from the second level heterostructure and the dual heterostructure, respectively. It is inferred that in the segment GH, only the second level heterostructure produces the strengthening effect, while after point H, the dual level heterostructure deforms cooperatively. When the applied stress is large enough, it will overcome the friction stresses and the HDI stress originating from dual heterostructure, to drive the dislocation forward again at the reloading yield point I (σ_r). Therefore, the HDI stress ($\sigma_{HDI-1st}$) contributed by the first-level heterostructure can be obtained by subtracting $\sigma_{HDI'}$ (i.e., $\sigma_{HDI-2nd}$) from the overall σ_{HDI}, that is:

$$\sigma_{HDI-1st} = \sigma_{HDI} - \sigma_{HDI'} \tag{5}$$

The specific values of HDI stress calculated at different strains are listed in Table 3. The value of $\sigma_{HDI-1st}$ is more than twice larger than that of $\sigma_{HDI-2nd}$ at the approximately same true strain, indicating that the first-level heterostructure is the main contributor to the

Table 3
The calculated HDI stresses for the HS1 nanocomposite at different true strains.

Samples \ True strain (%)	1	2	3	4
$\sigma_{HDI\text{-}HS1}$	191.6	202.1	214.6	215.4
$\sigma_{HDI\text{-}HS1\text{-}1st}$	130.2	134.7	145.8	146.4
$\sigma_{HDI\text{-}HS1\text{-}2nd}$	61.4	67.4	68.8	69.0

high strength of the HS1 nanocomposite. In contrast, after the RS and annealing treatment, nanoparticles dispersed homogeneously in the matrix, but then the inflection point is no longer distinguishable on the LUR curve for the HS2 sample.

3.3.3. Dislocation activities and strain hardening under plastic deformation

Fig. 9a, b and c show TEM images of the dual-heterostructured nanocomposite HS1 at a tensile strain of ~1.5 %, and it can be seen that the GNDs have been generated and accumulated locally in the CG Al lamellae near the zone interfaces. Meanwhile, no cracks were observed, because of the well bonded ductile/hard zone interfaces and the interphase interfaces. As shown in Fig. 9d, the dislocations are from a few active dislocation sources, and accumulate locally at grain boundaries. Consequently, the dislocation accumulation produces a back stress strong enough to stop the dislocation sources from emitting more dislocations. As a result, the strength of CG Al lamellae is elevated to a level that is unachievable by homogeneous CG Al.

In a short summary, HDI hardening in the dual-heterostructured nanocomposite evolved in the following way during the tensile deformation: Upon loading, both the ductile PFZs and hard PRZs (UFG Al + AlN) matrix deformed elastically, as schematically shown in Fig. 10a; With increasing strain, the ductile PFZs began to deform plastically while the nanoparticle-reinforced UFG Al matrix remained elastic, resulting in a strain gradient near the zone interfaces; GNDs were generated and accumulated in CG PFZs near the zone interfaces to accommodate the strain gradient, as illustrated in Fig. 10b; This produced strong back stress to strengthen the ductile CG PFZs, and thus increased the overall yield strength of the HS1 nanocomposite (Zhu, 2021a); With further straining, the dislocations in the hard PRZs were also activated to produce back stress but in the UFG matrix near nanoparticles, as depicted in Fig. 10c. This further increased the yield strength and strain hardening of the hard zones. Since the nanoparticles are un-deformable, the HDI stress in the nanoparticle-reinforced UFG zones was primarily caused by back stress as well. These two levels of HDI strengthening and strain hardening were produced in the hard zones by the dislocation interactions with nanoparticles, and by the incompatible deformation between the hard and ductile zones, which rendered the HS1 sample a superior combination of strength and ductility. Consequently, the HS1 sample is stronger than the HS2 sample, although the HS1 sample contains a higher fraction of coarse grains. In addition to HDI strengthening, it is also noted that the RS treatment broke the nanoparticle networks (Fig. 5), which also had a negative effect on the strength of the HS2 sample.

3.3.4. Strain distribution and evolution during tensile deformation

According to microstructural characterization and stress-strain analysis, the ductile zones in the dual-heterostructured AlN$_p$/Al
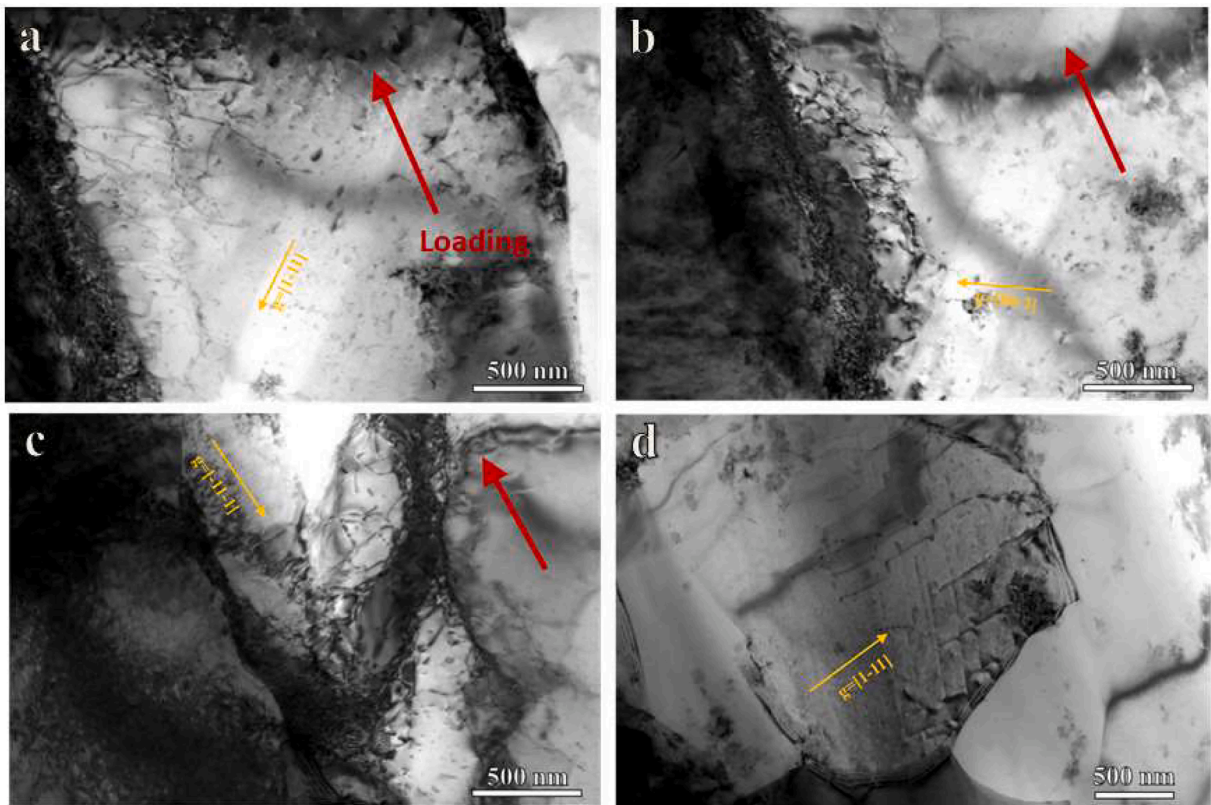
Fig. 9. Microstructures of the dual-heterostructured AlN$_p$/Al nanocomposites (HS1) at a tensile strain of 1.5 %: (a–c) TEM images show high densities of GNDs near interfaces between PRZs and PFZs, (d) TEM image shows GNDs in a micrometer-sized grain.
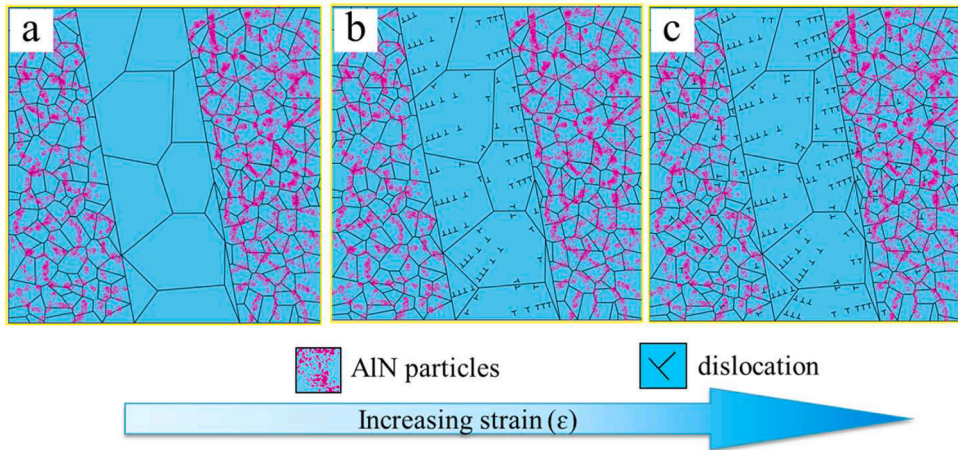
Fig. 10. Schematic illustration of the dislocation evolution behavior in the dual heterostructured aluminum matrix nanocomposites during deformation: (a) elastic deformation at the initial stage, (b) elastic-plastic deformation stage, (c) plastic deformation stage.

nanocomposites have sustained higher plastic strain than the hard zones. To support the credibility of the observed strain partitioning, we also performed strain measurement by digital image correlation to map the full-field strain distribution during tensile deformation. Fig. 11a and c shows the tensile specimens with painted surfaces. Fig. 11b shows the strain field of the HS1 nanocomposite within the gauge length at different tensile strains. At the initial stage of tensile plastic deformation (at strains of 0.005 % and 0.5 %), the strain is distributed uniformly throughout the entire loading area. At the strain of 1 %, strain localization occurred, resulting in the alternative distribution of high-strain and low-strain regions. This resembles the characteristic dispersive shear strain bands found in hetero-structured alloys (Liu et al., 2020a,b; Wang et al., 2020; Zhu and Wu, 2023). The evolution of the strain field in HS1 sample is markedly different from the conventional deformation behavior of metal matrix composites (Gao et al., 2017), such as the HS2 sample shown in Fig. 11d: At the early stages of plastic deformation, the strain distributed uniformly within the gauge length; At the total strain of 1 %, the strain starts to localize in just one narrow region, resulting in necking and fracture of the tensile sample at the strain higher than 1.5 %. The strain delocalization effect seen in the HS1 sample is attributed to the dual-heterostructure setup.

The evolution of local strain in a PRZ has been mapped by the high-resolution SEM-DIC, as shown in Fig. 12. Fig. 12a and b shows the local strain fields $\varepsilon_{xx} = du_x/dx$ and $\varepsilon_{yy} = du_y/dy$ at different tensile strains. At the tensile strain of 0.5 %, both the strain distri-butions of ε_{xx} and ε_{yy} are uniform across the entire surface of the study. When the tensile strain increased to ~3.8 %, microscopic strain localizations occurred for both ε_{xx} and ε_{yy}, resulting in many dispersed and crossed strain bands as shown in Fig. 12a and b. Many of the discrete strain bands were also developed at about 45° to the loading direction and the widths of these strain bands are about 10 μm. The high density and closely spaced strain bands effectively delayed macroscopic strain concentration that normally occurred in conventional metal matrix composites (MMCs) (Huang et al., 2018). Therefore, the well-developed discrete microscopic strain bands contributed to the enhanced ductility of the dual heterostructured nanocomposite.

Notwithstanding, the main point is that the heterostructures lead to the dispersive shear strain bands during the early stage of plastic deformation till the strain is larger than 4 % (Fig. S5), thus resulting in delayed macroscopic strain localization and enhanced strain hardening capability and ductility. The PRZs render the nanocomposite the high strength, while the ductile PFZs render the nanocomposite the decent ductility. Such a combination brings about a good balance of high strength and high ductility to particle reinforced MMCs.

3.3.5. Surface morphology evolution

The evolution of the surface morphology for the HS1 sample was analyzed via in-situ SEM tensile deformation. Fig. 13 shows snapshots of the deformation process. The initial appearance of the tensile specimen is shown in Fig. 13a. A typical region containing PRZs and PFZs has been selected for observation as shown in Fig. 13a1. At the strain of 0.8 %, a slip band (marked by the blue arrow in Fig. 13a2) was observed in the PFZs, indicating that the plastic deformation has begun in the ductile PFZs. When the strain was increased to ~3.8 %, many near parallel slip bands appeared at about 45° to the tensile direction in the ductile PFZs, while there were no obvious deformation bands in the hard PRZs. However, some micro voids formed in the hard PRZs (marked by the yellow circle in Fig. 13a3). When the strain reached ~8.6 %, the specimen necked. There are enormous amounts of slip bands closely spaced in the ductile zone, suggesting effective plastic deformation in the PFZs. In contrast, high densities of closely spaced microcracks are seen in the PRZs as shown in Fig. 13a4. Apparently, the PFZs are far more ductile than the PRZs.

Fig. 13b and c show the macroscopic fracture morphology of the HS1 sample. In an enlarged view of the area adjacent to the fracture tip, there are a lot of micro voids (as indicated by the yellow circles in Fig. 13d) initiated at and propagated along the interfaces between AlN nanoparticles and the matrix in the PRZs. However, the most pronounced feature is the high densities of microcracks dispersed in the PRZs, as indicated by the white arrows in Fig. 13d and e. Most of the microcracks are only a few micrometers in length, but some microcracks can have lengths of more than ten micrometers as indicated by the green arrows in Fig. 13d. Notwithstanding,
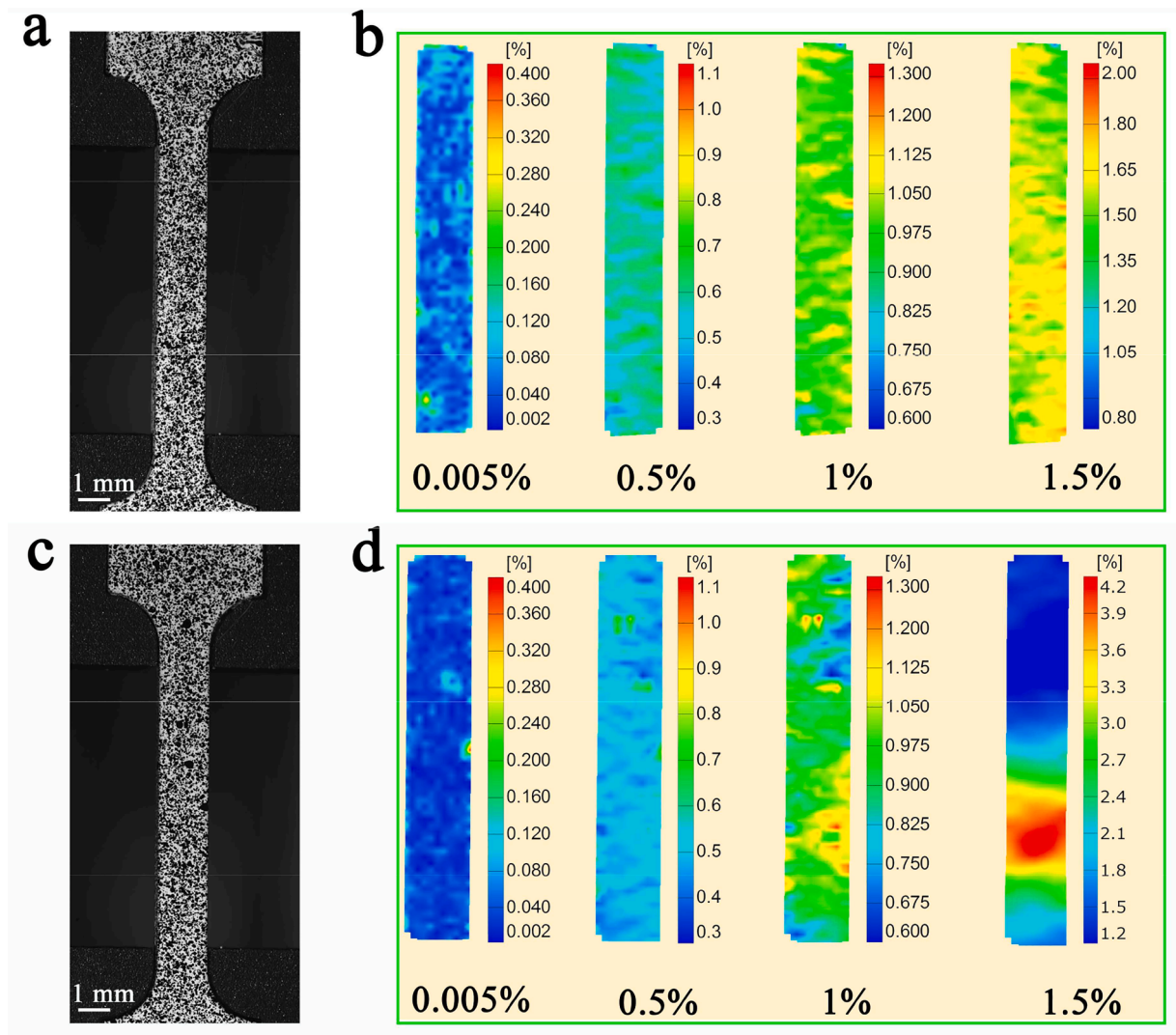
Fig. 11. The strain analysis of AlN$_P$/Al nanocomposites during the tensile test: (a, c) the HS1 and HS2 tensile specimens with painted surfaces, (b) the strain field distributions at the initial stages of tensile plastic deformation on HS1 sample and (d) HS2 samples.

the microcracks were effectively contained in the PRZs by the zone boundaries between PFZs and PRZs. For example, as indicated by the pink arrows in Fig. 13d, f, g and h, no matter how long the microcracks are, they always terminate at zone boundaries between PFZs and PRZs. This is because the ductile CG PFZs is very effective in blunting the crack tips (Ovid'ko et al., 2018), by emitting dislocations in the coarse Al grains. The surface morphology of the region away from the fracture tip is shown in Fig. 13e; Again, there are high densities of dispersed microcracks (white arrows) and many voids (yellow circles) in the PRZs, indicating that dispersive microcracks and voids are the major strain carriers when plastic instability is triggered.

Dispersive microcracks have recently attracted researchers' attention, because they have been related to dramatic improvements in fracture toughness and fatigue resistance for metallic materials (Chen et al., 2008; Koyama et al., 2017; Niu et al., 2022). It is worth noting that so far the dispersive microcracks have only been observed in heterostructured materials including both metallic materials (Chen et al., 2008) and natural composite materials such as bones (Koyama et al., 2017). Although the strain rates and stresses encountered in fracture toughness and fatigue tests are different from those in quasi-static tensile tests, the nature of cracks is the same: cracks are a kind of plastic instability that releases the local stresses. Once cracks nucleated, the stress would drop due to stress release. However, strain hardening naturally occurs at crack tips and other intact regions can more or less compromise the stress released by cracks. Therefore, theoretically speaking if the stress increase due to strain hardening is higher than the stress release due to cracks, overall strain hardening for the bulk material is possible despite different plastic deformation modes e.g., impact, fatigue and quasi-static tension. For homogeneous CG materials, once cracks nucleated, they could quickly coalesce into large macroscopic cracks that are impossible to be stopped by strain hardening; In contrast, the microcracks seen in heterostructured materials are very likely to be stopped or delayed by ductile zones with high strain hardening capabilities. This phenomenon makes us wonder if the bulk material
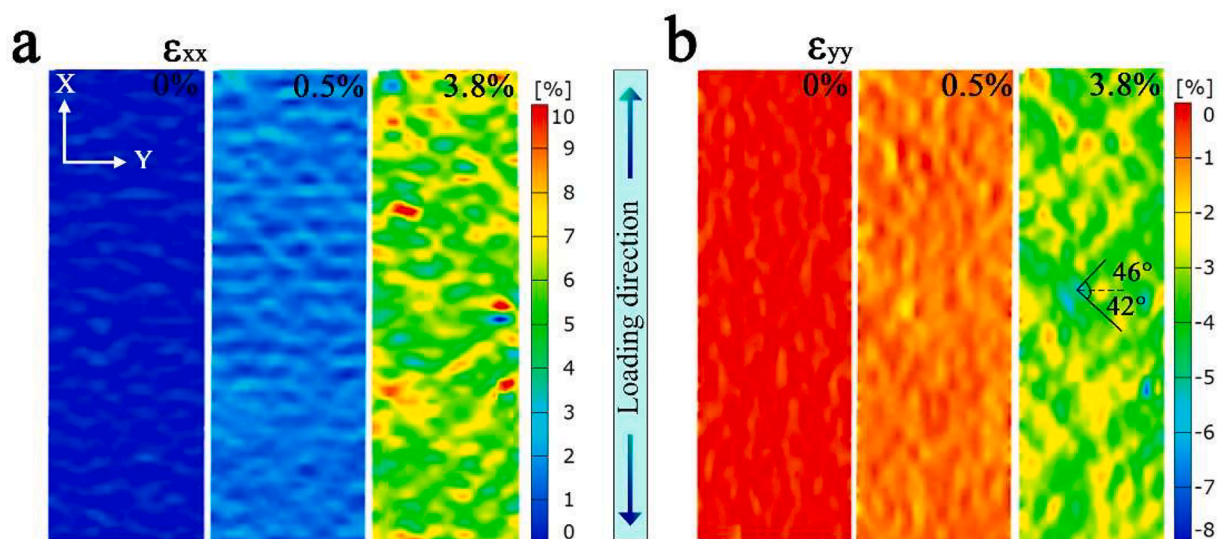
Fig. 12. Snapshots of in-situ strain field mapping for a PRZ in the HS1 nanocomposite: the distribution of tensile strain ε_{xx} (a) and shrinking strain ε_{yy} (b) X is the tensile direction and Y is the width direction of the sample. Applied tensile strain is provided on the top right corner of each map. The black lines in (b) mark the shear banding direction and the black arrows mark the dispersed shear strain bands.

can still demonstrate overall strain hardening once dispersive microcracks occur. We have to leave this question open here while relevant experiments are still underway, but according to available literature (Chen et al., 2008; Koyama et al., 2017; Niu et al., 2022) and current results we can conclude that the dispersive microcracks can effectively delay catastrophic failure and prolong the plastic deformation process.

4. Conclusions

Overcoming the longstanding challenge of strength-ductility trade-off is of pivotal importance for metal matrix composite. Here, we propose a dual-heterostructure design strategy to distribute the reinforcement particles non-uniformly in a dual-level hierarchy, which is contrary to the traditional approach of uniform dispersion of nanoparticles in AMCs. A dual-heterostructured Al matrix nanocomposite has been successfully fabricated, featuring ductile fibrous CG PFZs embedded in hard UFG PRZs. It is found that the dual-heterostructured Al matrix composite achieved a strength-ductility combination along the ED that is superior to the UFG composite with a uniform dispersion of nanoparticles. Different from early reported heterostructures, the dual heterostructure produced HDI strengthening and hardening in two levels. The dual level HDI strengthening effect has been reflected by the inflection points on the LUR stress-strain curves, which are revealed for the first time. Furthermore, the evolution of the local strain field analyzed by the SEM in-situ tensile test directly proved that the local strain partitioning occurred. Hence, the ductile PFZs have carried a larger strain than the hard PRZs. At the microscale, dispersive shear strain bands, i.e., alternating distribution of the high strain and low strain regions are seen in the PRZs, helping delay macroscopic strain localization. These findings point to a new horizon for designing novel AMCs with superior mechanical properties.

CRediT authorship contribution statement

Jinfeng Nie: Conceptualization, Methodology, Data curation, Writing – review & editing, Funding acquisition. **Yuyao Chen:** Methodology, Investigation, Data curation, Writing – original draft. **Lei Song:** Methodology, Data curation, Investigation. **Yong Fan:** Data curation. **Yang Cao:** Writing – review & editing. **Kewei Xie:** Methodology. **Sida Liu:** Data curation. **Xiangfa Liu:** Methodology, Supervision. **Yonghao Zhao:** Writing – review & editing. **Yuntian Zhu:** Conceptualization, Writing – review & editing, Funding acquisition, Supervision.

Declaration of Competing Interest

The authors declare that they have no known competing financial interests or personal relationships that could have appeared to influence the work reported in this paper.

Data availability

All data included in this study are available upon request by contact with the corresponding author.
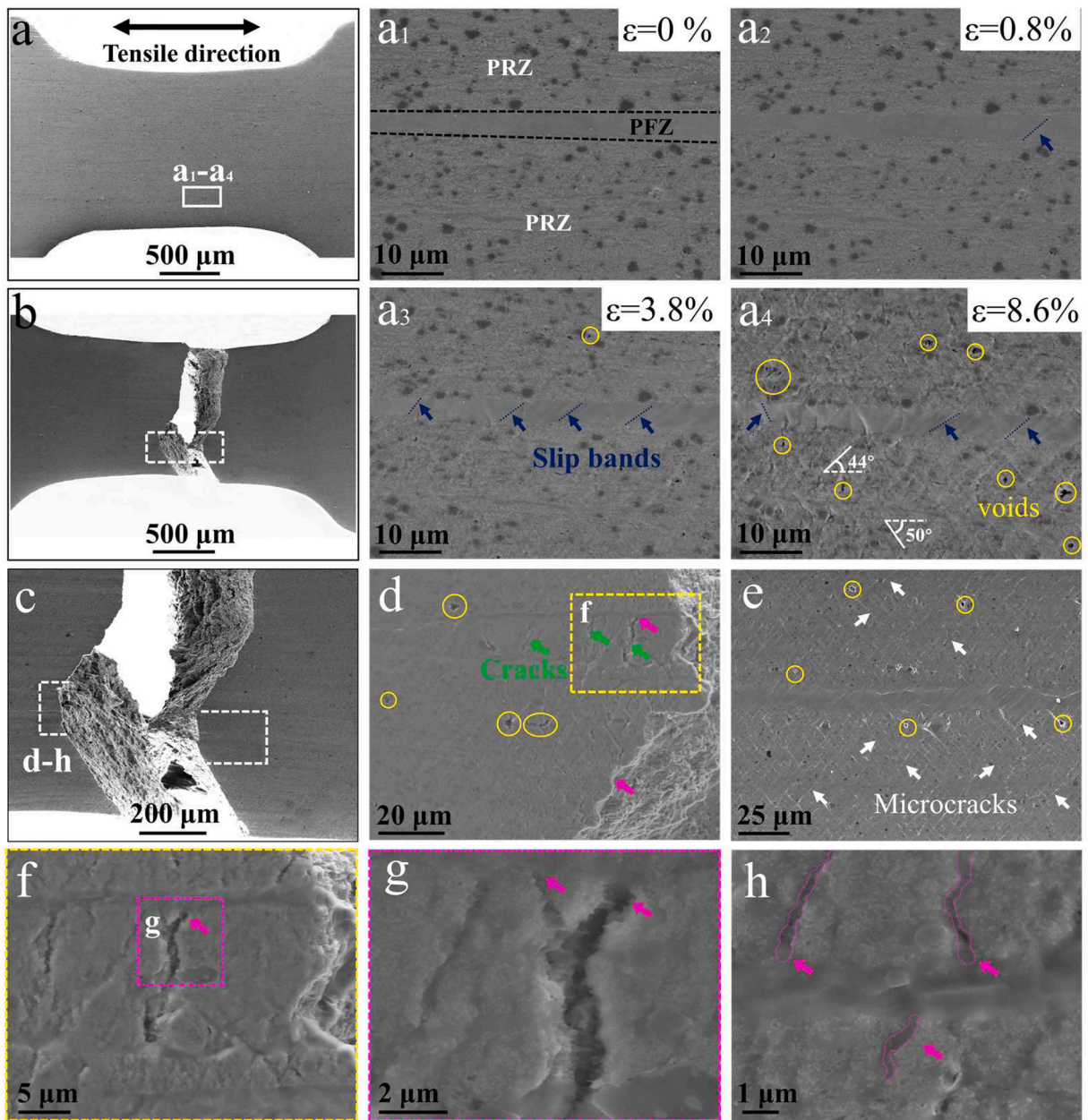
Fig. 13. The deformation and fracture mechanisms of the HS1 nanocomposite: (a) the in-situ tensile specimen, (a_1–a_4) SEM images showing the surface morphology evolution with the increasing strain, (b) macroscopic fracture morphology of the tensile sample, (c) enlarged view of the white-boxed area in Fig. 13b, (d) the surface morphology near the fracture tip, (e) the surface morphology away from the fracture tip, (f–h) enlarged images showing the propagation and blunting of cracks.

Supplementary materials

Supplementary material associated with this article can be found, in the online version, at doi:10.1016/j.ijplas.2023.103825.

References

Aikin, R.M., Christodoulou, l., 1991. The role of equiaxed particles on the yield stress of composites. Scr. Metal. Mater. 25, 9–14.

Ashok Kumar, B., Murugan, N., 2012. Metallurgical and mechanical characterization of stir cast AA6061-T6-AlNp composite. Mater. Des. 40, 52–58.

Bate, P.S., Knutsen, R.D., Brough, I., Humpherys, F.J., 2005. The characterization of low-angle boundaries by EBSD. J. Microsc. 220 (1), 36–46.

Calcagnotto, M., Ponge, D., Demir, E., Raabe, D., 2010. Orientation gradients and geometrically necessary dislocations in ultrafine grained dual-phase steels studied by 2D and 3D EBSD. Mater. Sci. Eng. A 527 (10), 2738–2746.

Chen, A.Y., Li, D.F., Zhang, J.B., Song, H.W., Lu, J., 2008. Make nanostructured metal exceptionally tough by introducing non-localized fracture behaviors. Scr. Mater. 59, 579–582.

Chen, F., Mei, Q.S., Li, J.Y., Li, C.L., Wan, L., Mei, X.M., Chen, Z.H., Xu, T., Wang, Y.C., Tan, Y.Y., 2022. Achieving synergistic strengthening and enhanced comprehensive properties of Cu matrix composites at high strength level by incorporating nanocarbons and Al_2O_3 dual reinforcements. Mater. Sci. Eng. A 839, 142859.

Chen, H., Zhang, M., Kong, F.X., Li, B., Cui, X.F., Huang, Y.D., Hort, N., Willumeit-Römer, R., Xie, W.D., Wei, G.B., 2023. Effect of extrusion and rotary swaging on the microstructural evolution and properties of Mg-5Li-5.3Al-0.7Si alloy. Mater. Sci. Eng. A 885, 145627.

Chen, L.Y., Xu, J.Q., Choi, H., Pozuelo, M., Ma, X., Bhowmick, S., Yang, J.M., Mathaudhu, S., Li, X.C., 2015. Processing and properties of magnesium containing a dense uniform dispersion of nanoparticles. Nature 528, 539–543.

Derrien, K., Baptiste, D., Guedra-Degeorges, D., Foulquier, J., 1999. Multiscale modeling of the damaged plastic behavior and failure of Al/SiCp composites. Int. J. Plast. 15, 667–685.

Dickson, J.I., Boutin, J., Handfield, L., 1984. A comparison of two simple methods for measuring cyclic internal and effective stresses. Mater. Sci. Eng. A 64, L7–L11.

Ding, C., Yu, K., Nodooshan, H.R.J., Ye, S., Yu, P., 2022. Effect of powder microstructure on the thermal and mechanical properties of hot extruded Al-CNT composite. J. Alloys Compd. 891, 162059.

Dong, Z., Ma, Z.Q., Liu, Y.C., 2021. Accelerated sintering of high-performance oxide dispersion strengthened alloy at low temperature. Acta Mater. 220, 117309.

Fattahi, M., Mohammady, M., Sajjadi, N., Honarmand, M., Fattahi, Y., Akhavan, S., 2015. Effect of TiC nanoparticles on the microstructure and mechanical properties of gas tungsten arc welded aluminum joints. J. Mater. Process. Technol. 217, 21–29.

Fournier, B., Sauzay, M., Caës, C., Noblecourt, M., Mottot, M., 2006a. Analysis of the hysteresis loops of a martensitic steel: part I: study of the influence of strain amplitude and temperature under pure fatigue loadings using an enhanced stress partitioning method. Mater. Sci. Eng. A 437, 183–196.

Fournier, B., Sauzay, M., Caës, C., Mottot, M., Noblecourt, M., Pineau, A., 2006b. Analysis of the hysteresis loops of a martensitic steel: part II: study of the influence of creep and stress relaxation holding times on cyclic behaviour. Mater. Sci. Eng. A 437, 197–211.

Gallet, J., Perez, M., Guillou, R., Ernould, C., Le Bourlot, C., Langlois, C., Beausir, B., Bouzy, E., Chaise, T., Cazottes, S., 2023. Experimental measurement of dislocation density in metallic materials: a quantitative comparison between measurements techniques (XRD, R-ECCI, HR-EBSD, TEM). Mater. Charact. 199, 112842.

Gao, H., 1999. Mechanism-based strain gradient plasticity? I. Theory. J. Mech. Phys. Solids 47, 1239–1263.

Gao, X.Z., Lu, Y.P., Zhang, B., Liang, N.N., Wu, G.Z., Sha, G., Liu, J.Z., Zhao, Y.H., 2017. Microstructural origins of high strength and high ductility in an AlCoCrFeNi2.1 eutectic high-entropy alloy. Acta Mater. 141, 59–66.

Geng, J.W., Li, Y.G., Wang, F.F., Wang, Z.P., Xia, P.K., Li, X.F., Chen, D., Wang, M.L., Wang, H.W., 2023. Cyclic deformation and dynamically induced short-range ordering in small particles reinforced Al composite. Int. J. Plast. 163, 103568.

Guo, H., Zhang, Z.W., Zhang, Y., Cui, Y., Sun, L.X., Chen, D., 2020. Improving the mechanical properties of B_4C/Al composites by solid-state interfacial reaction. J. Alloys Compd. 829, 154521.

Hasan, M.N., Liu, Y.F., An, X.H., Gu, J., Song, M., Cao, Y., Li, Y.S., Zhu, Y.T., Liao, X.Z., 2019. Simultaneously enhancing strength and ductility of a high-entropy alloy via gradient hierarchical microstructures. Int. J. Plast. 123, 178–195.

Horton, J.A., Ohr, S.M., 1982. TEM observations of dislocation emission at crack tips in aluminum. J. Mater. Sci. 17, 3140–3148.

Hu, C.M., Lai, C.M., Du, X.H., Ho, N.J., Huang, J.C., 2008. Enhanced tensile plasticity in ultrafine-grained metallic composite fabricated by friction stir process. Scr. Mater. 59, 1163–1166.

Huang, C.X., Wang, Y.F., Ma, X.L., Yin, S., Hoppel, H.W., Goken, M., Wu, X.L., Gao, H.J., Zhu, Y.T., 2018. Interface affected zone for optimal strength and ductility in heterogeneous laminate. Mater. Today 21, 713–719.

Huang, L.J., Geng, L., Peng, H.X., 2015. Microstructurally inhomogeneous composites: is a homogeneous reinforcement distribution optimal? Prog. Mater. Sci. 71, 93–168.

Jiang, L., Wen, H.M., Yang, H.R., Hu, T., Topping, T., Zhang, D.L., Lavernia, E.J., Schoenung, J.M., 2015. Influence of length-scales on spatial distribution and interfacial characteristics of B_4C in a nanostructured Al matrix. Acta Mater. 89, 327–343.

Jiang, L., Yang, H., Yee, J.K., Mo, X., Topping, T., Lavernia, E.J., Schoenung, J.M., 2016. Toughening of aluminum matrix nanocomposites via spatial arrays of boron carbide spherical nanoparticles. Acta Mater. 103, 128–140.

Kai, X.Z., Huang, S.M., Wu, L., Tao, R., Peng, Y.J., Mao, Z.M., Chen, F., Li, G.R., Chen, G., Zhao, Y.T., 2019. High strength and high creep resistant ZrB_2/Al nanocomposites fabricated by ultrasonic-chemical in-situ reaction. J. Mater. Sci. Technol. 35, 2107–2114.

Kang, Y.C., Chan, S.L.I., 2004. Tensile properties of nanometric Al_2O_3 particulate-reinforced aluminum matrix composites. Mater. Chem. Phys. 85, 438–443.

Kim, T.W., 2006. Heterogeneous void distribution in aluminum metal matrix composites and its effect on deformation-failure processes. Scr. Mater. 55, 1115–1118.

Koyama, M., Zhang, Z., Wang, M., Ponge, D., Raabe, D., Tsuzaki, K., Noguchi, H., Tasan, C.C., 2017. Bone-like crack resistance in hierarchical metastable nanolaminate steels. Science 355, 1055–1057.

Li, M.Q., Wang, S.K., Wang, Q.H., Zhao, Z.H., Duan, C.Y., Zhao, D., Zhang, L.Z., Wang, Y., 2020a. Microstructure and mechanical properties of MoAlB particles reinforced Al matrix composites by interface modification with in situ formed Al12Mo. J. Alloys Compd. 823, 153813.

Li, J.J., Lu, W.J., Chen, S.H., Liu, C.H., 2020b. Revealing extra strengthening and strain hardening in heterogeneous two-phase nanostructures. Int. J. Plast. 126, 102626.

Li, Z., Fan, G.L., Guo, Q., Li, Z.Q., Su, Y.S., Zhang, D., 2015a. Synergistic strengthening effect of graphene-carbon nanotube hybrid structure in aluminum matrix composites. Carbon 95, 419–427.

Li, Z., Guo, Q., Li, Z., Fan, G., Xiong, D.B., Su, Y., Zhang, J., Zhang, D., 2015b. Enhanced mechanical properties of graphene (reduced graphene oxide)/aluminum composites with a bioinspired nanolaminated structure. Nano Lett. 15, 8077–8083.

Li, P.Y., Li, X.N., Liu, Z.Y., Chen, L.Q., Xiao, B.L., Ma, Z.Y., 2022. Enhanced strength-ductility synergy of carbon nanotube/Al-Cu-Mg composites via introducing laminate structure and grain modification. Compos. B Eng. 243, 110178.

Liu, J., Chen, Z., Zhang, F.G., Ji, G., Wang, M.L., Ma, Y., Ji, V., Zhong, S.Y., Wu, Y., Wang, H.W., 2018a. Simultaneously increasing strength and ductility of nanoparticles reinforced Al composites via accumulative orthogonal extrusion process. Mater. Res. Lett. 6, 406–412.

Liu, X.L., Yuan, F.P., Zhu, Y.T., Wu, X.L., 2018b. Extraordinary Bauschinger effect in gradient structured copper. Scr. Mater. 150, 57–60.

Liu, X.Q., Li, C.J., You, X., Xu, Z.Y., Li, X., Bao, R., Tao, J.M., Yi, J.H., 2020a. Size-dependent effects of Ti powders in the pure aluminum matrix composites reinforced by carbon nanotubes. J. Alloys Compd. 823, 153824.

Liu, Y.F., Cao, Y., Mao, Q.Z., Zhou, H., Zhao, Y.H., Jiang, W., Liu, Y., Wang, J.T., You, Z.S., Zhu, Y.T., 2020b. Critical microstructures and defects in heterostructured materials and their effects on mechanical properties. Acta Mater. 189, 129–144.

Liu, S.S., Xia, D.B., Yang, H., Huang, G.S., Yang, F.X., Chen, X.H., Tang, A.T., Jiang, B., Pan, F.S., 2022. Mechanical properties and deformation mechanism in Mg-Gd alloy laminate with dual-heterostructure grain size and texture. Int. J. Plast. 157, 103371.

Luo, X., Zhao, K., He, X., Bai, Y.L., De Andrade, V., Zaiser, M., An, L.N., Liu, J.L., 2022. Evading strength and ductility trade-off in an inverse nacre structured magnesium matrix nanocomposite. Acta Mater. 228, 117730.

Ma, K., Wen, H., Hu, T., Topping, T.D., Isheim, D., Seidman, D.N., Lavernia, E.J., Schoenung, J.M., 2014. Mechanical behavior and strengthening mechanisms in ultrafine grain precipitation-strengthened aluminum alloy. Acta Mater 62, 141–155.

Ma, Y., Chen, H., Zhang, M.X., Addad, A., Kong, Y., Lezaack, M.B., Gan, W., Chen, Z., Ji, G., 2023. Break through the strength-ductility trade-off dilemma in aluminum matrix composites via precipitation-assisted interface tailoring. Acta Mater. 242, 118470.

Mavlyutov, A.M., Latynina, T.A., Murashkin, M.Y., Valiev, R.Z., Orlova, T.S., 2017. Effect of annealing on the microstructure and mechanical properties of ultrafine-grained commercially pure Al. Phys. Solid State 59, 1970–1977.

Najimi, A.A., Shahverdi, H.R., 2017. Effect of milling methods on microstructures and mechanical properties of Al6061-CNT composite fabricated by spark plasma sintering. Mater. Sci. Eng. A 702, 87–95.

Nie, J.F., Chen, Y.Y., Chen, X., Liu, X.F., Liu, G.L., Zhao, Y.H., Zhu, Y.T., 2020. Stiff, strong and ductile heterostructured aluminum composites reinforced with oriented nanoplatelets. Scr. Mater. 189, 140–144.

Nie, J.F., Liu, Y.F., Wang, F., Zhou, H., Cao, Y., Liu, X.F., An, X.H., Liao, X.Z., Zhu, Y.T., Zhao, Y.H., 2021. Key roles of particles in grain refinement and material strengthening for an aluminum matrix composite. Mater. Sci. Eng. A 801, 140414.

Niu, G., Zurob, H.S.S., Misra, R.D.K., Tang, Q.B., Zhang, Z.H., Nguyen, M.T., Wang, L.L., Wu, H.B., Zou, Y., 2022. Superior fracture toughness in a high-strength austenitic steel with heterogeneous lamellar microstructure. Acta Mater. 226, 117642.

Orowan, E., 1947. Classification and nomenclature of internal stresses. J. Inst. Met. 73, 47–59.

Ovid'ko, I.A., Sheinerman, A.G., 2009. Grain size effect on crack blunting in nanocrystalline materials. Scr. Mater. 60, 627–630.

Ovid'ko, I.A., Sheinerman, A.G., 2010. Ductile vs. brittle behavior of pre-cracked nanocrystalline and ultrafine-grained materials. Acta Mater. 58, 5286–5294.

Ovid'ko, I.A., Valiev, R.Z., Zhu, Y.T., 2018. Review on superior strength and enhanced ductility of metallic nanomaterials. Prog. Mater Sci. 94, 462–540.

Ren, L., Gao, T., Nie, J., Liu, G., Liu, X., 2022. A novel core-shell TiCx particle by modifying TiCx with B element and the preparation of the (TiCx + AlN)/Al composite. J. Alloys Compd. 894, 162448.

Rice, J.R., Thomson, R., 2006. Ductile versus brittle behaviour of crystals. Philos. Mag. 29, 73–97.

Rong, X.D., Zhao, D.D., Chen, X.F., Zhang, X., Wan, D., Shi, C.S., He, C.N., Zhao, N.Q., 2023. Towards the work hardening and strain delocalization achieved via in-situ intragranular reinforcement in Al-CuO composite. Acta Mater. 256, 119110.

Seok, M.Y., Lee, J.A., Lee, D.H., Ramamurty, U., Nambu, S., Koseki, T., Jang, J.i., 2016. Decoupling the contributions of constituent layers to the strength and ductility of a multi-layered steel. Acta Mater. 121, 164–172.

Shao, C., Zhao, S., Wang, X., Zhu, Y., Ritchie, R.O., 2019. Architecture of high-strength aluminum-matrix composites processed by a novel microcasting technique. NPG Asia Mater. 11, 69.

Shen, Q., Yuan, Z., Liu, H., Zhang, X., Fu, Q., Wang, Q., 2020. The damage mechanism of 17 vol.%SiCp/Al composite under uniaxial tensile stress. Mater. Sci. Eng. A 782, 139274.

Sitarama Raju, K., Subramanya Sarma, V., Kauffmann, A., Hegedűs, Z., Gubicza, J., Peterlechner, M., Freudenberger, J., Wilde, G., 2013. High strength and ductile ultrafine-grained Cu-Ag alloy through bimodal grain size, dislocation density and solute distribution. Acta Mater. 61, 228–238.

Sun, H., Saba, F., Fan, G.L., Tan, Z.Q., Li, Z.Q., 2022. Micro/nano-reinforcements in bimodal-grained matrix: a heterostructure strategy for toughening particulate reinforced metal matrix composites. Scr. Mater. 217, 114774.

Teng, H.Y., Tan, Z.Q., Zhao, X.H., Fan, G.L., Yue, Z.M., Li, Z.Q., Xiong, D.B., 2023. Simultaneously enhanced strength and ductility in graphene nanosheet/Al-Cu-Mg nano-laminated composites by incorporating coarse domains. Mater. Res. Lett. 11, 143–151.

Wahab, M.N., Ghazali, M.J., Daud, A.R., 2011. Effect of aging treatment on microstructure and mechanical properties of Al-Si matrix alloy reinforced with high purity aluminum nitride (AlN). Key. Mater. 462–463, 967–971.

Wang, G., Zhang, Y.M., Zou, B.K., Liu, Y., Zheng, S.Q., Li, X.C., Yan, W.T., Li, Z., Wang, Y.M., 2023. Enhanced plasticity due to melt pool flow induced uniform dispersion of reinforcing particles in additively manufactured metallic composites. Int. J. Plast. 164, 103591.

Wang, H., Zhang, H.M., Cheng, X.W., Liu, L., Chang, S., Mu, X.N., Ge, Y.X., 2022. Microstructure and mechanical properties of GNPs and in-situ TiB hybrid reinforced Ti-6Al-4V matrix composites with 3D network architecture. Mater. Sci. Eng. A 854, 143536.

Wang, Y.F., Huang, C.X., Li, Y.S., Guo, F.J., He, Q., Wang, M.S., Wu, X.L., Scattergood, R.O., Zhu, Y.T., 2020. Dense dispersed shear bands in gradient-structured Ni. Int. J. Plast. 124, 186–198.

Wauthier-Monnin, A., Chauveau, T., Castelnau, O., Réglé, H., Bacroix, B., 2015. The evolution with strain of the stored energy in different texture components of cold-rolled IF steel revealed by high resolution X-ray diffraction. Mater. Charact. 104, 31–41.

Wu, H., Huang, M., Li, X., Xia, Y., Wang, Z., Fan, G., 2021. Temperature-dependent reversed fracture behavior of multilayered TiBw/Ti-Ti (Al) composites. Int. J. Plast. 141.

Wu, X., Yang, M., Yuan, F., Wu, G., Wei, Y., Huang, X., Zhu, Y., 2015. Heterogeneous lamella structure unites ultrafine-grain strength with coarse-grain ductility. Proc. Natl. Acad. Sci. USA 112, 14501–14505.

Wu, H., Huang, M., Xia, Y.P., Li, X.W., Li, R.G., Liu, C.L., Gan, W.M., Xiao, T.Q., Geng, L., Liu, Q., Fan, G.H., 2023. The importance of interfacial stress-affected zone in evading the strength-ductility trade-off of heterogeneous multi-layered composites. Int. J. Plast. 160, 103485.

Xia, Y.P., Miao, K.S., Wu, H., Geng, L., Xu, C., Ku, C.S., Fan, G.H., 2022. Superior strength-ductility synergy of layered aluminum under uniaxial tensile loading: the roles of local stress state and local strain state. Int. J. Plast. 152, 103240.

Xiang, Y., Vlassak, J.J., 2005. Bauschinger effect in thin metal films. Scr. Mater. 53, 177–182.

Xing, Y., Li, N.Y., Li, C.J., Gao, P., Guan, H.D., Yang, C.M.Y., Pu, C.J., Yi, J.H., 2022. Effects of size and oxidation treatment for SiC particles on the microstructures and mechanical properties of SiCp/Al composites prepared by powder metallurgy. Mater. Sci. Eng. A 851, 143664.

Yang, K.M., Ma, Y.C., Zhang, Z.Y., Zhu, J., Sun, Z.B., Chen, J.S., Zhao, H.H., Song, J., Li, Q., Chen, N.Q., Ma, H.Y., Zhou, J., Liu, Y., Fan, T.X., 2020. Anisotropic thermal conductivity and associated heat transport mechanism in roll-to-roll graphene reinforced copper matrix composites. Acta Mater. 197, 342–354.

Yang, M.X., Pan, Y., Yuan, F.P., Zhu, Y.T., Wu, X.L., 2016. Back stress strengthening and strain hardening in gradient structure. Mater. Res. Lett. 4, 145–151.

Yang, M., Yan, D., Yuan, F., Jiang, P., Ma, E., Wu, X., 2018. Dynamically reinforced heterogeneous grain structure prolongs ductility in a medium-entropy alloy with gigapascal yield strength. Proc. Natl. Acad. Sci. USA 115, 7224–7229.

Yu, P., Balog, M., Yan, M., Schaffer, G.B., Qian, M., 2011. In situ fabrication and mechanical properties of Al-AlN composite by hot extrusion of partially nitrided AA6061 powder. J. Mater. Res. 26, 1719–1725.

Zan, Y.N., Zhou, Y.T., Liu, Z.Y., Ma, G.N., Wang, D., Wang, Q.Z., Wang, W.G., Xiao, B.L., Ma, Z.Y., 2019. Enhancing strength and ductility synergy through heterogeneous structure design in nanoscale Al2O3 particulate reinforced Al composites. Mater. Des. 166, 107629.

Zan, Y.N., Zhou, Y.T., Liu, Z.Y., Wang, Q.Z., Wang, W.G., Wang, D., Xiao, B.L., Ma, Z.Y., 2020. Microstructure and mechanical properties of (B4C+Al2O3)/Al composites designed for neutron absorbing materials with both structural and functional usages. Mater. Sci. Eng. A 773, 138840.

Zhang, Y., Yu, Y., Wang, L., Li, Y., Lin, F., Yan, W., 2022. Dispersion of reinforcing micro-particles in the powder bed fusion additive manufacturing of metal matrix composites. Acta Mater. 235, 118086.

Zhang, Z.M., Fan, G.L., Tan, Z.Q., Zhao, H.T., Xu, Y.J., Xiong, D.B., Li, Z.Q., 2021. Bioinspired multiscale Al2O3-rGO/Al laminated composites with superior mechanical properties. Compos. Part B 217, 108916.

Zhong, S.X., Xu, C., Li, Y., Li, W., Luo, H., Peng, R.Z., Jia, X.S., 2022. Hierarchy modification induced exceptional cryogenic strength, ductility and toughness combinations in an asymmetrical-rolled heterogeneous-grained high manganese steel. Int. J. Plast. 154, 103316.

Zhu, Y.T., Wu, X.L., 2023. Heterostructured materials. Prog. Mater. Sci. 131, 101019.

Zhu, Y.T., 2021a. Introduction to Heterostructured materials: a fast emerging field. Metall. Mater. Trans. A 52, 4715–4726.

Zhu, Y.T., Ameyama, K., Anderson, P.M., Beyerlein, I.J., Gao, H.J., Kim, H.S., Lavernia, E., Mathaudhu, S., Mughrabi, H., Ritchie, R.O., Tsuji, N., Zhang, X.Y., Wu, X.L., 2021b. Heterostructured materials: superior properties from hetero-zone interaction. Mater. Res. Lett. 9, 1–31.

Zhu, Y.T., Wu, X.L., 2019. Perspective on hetero-deformation induced (HDI) hardening and back stress. Mater. Res. Lett. 7, 393–398.